Aus dem Institut für kardiovaskuläre Computer-assistierte Medizin der
Medizinischen Fakultät Charité – Universitätsmedizin Berlin

DISSERTATION

Statistische Untersuchung von statischen Druck und Wandschubspannungsverteilungen der Strömung der Nasenatmung basierend auf der numerischen Strömungsberechnung

zur Erlangung des akademischen Grades

Doctor rerum medicinalium (Dr. rer. medic.)

vorgelegt der Medizinischen Fakultät

Charité – Universitätsmedizin Berlin

von

Jan Brüning (geb. Osman)

aus Berlin, Deutschland

Datum der Promotion: 18.12.2020

Inhaltsverzeichnis

1 Synopsis

1.1 Zusammenfassung

Bis zu 30 Prozent der Bevölkerung leidet unter Nasenatmungsbehinderungen, deren Ursache häufig eine gestörte Durchströmung der Nase in Folge morphologischer Veränderungen in der Nasenhöhle ist. Trotz dieser Prävalenz existiert bis heute kein allgemein akzeptiertes Modell, welches eine gesunde Nasenatmung von einer gestörten unterscheidet. Existierende Messmethoden erlauben lediglich das Erfassen integraler Maße wie bspw. des Nasenatemwiderstandes und sind somit nur bedingt geeignet die Strömung in der sehr komplexen, verwundenen Anatomie der Nasenhöhle zu untersuchen.

Die medizinische Bildgebung, insbesondere die Computertomographie, ermöglicht eine räumlich aufgelöste Abbildung dieser komplexen Anatomie. Die Kenntnis der patientenspezifischen Geometrie der Nasenhöhle erlaubt die Berechnung der patientenspezifischen Atemströmung mittels bildbasierter Strömungssimulationen. Dieser Ansatz ermöglicht die räumlich und zeitlich hochaufgelöste Simulation relevanter Strömungsparameter der Nasenatmung.

Der Fokus dieser Dissertation lag dabei auf der Entwicklung einer Methode, welche unter Verwendung der bildbasierten Simulation der Nasenatmung eine statistische Unterscheidung der Nasenatmung von gesunden Probanden und Patienten, die unter einer Nasenatmungsbehinderung leiden, erlaubt. Hierfür wurde zunächst in einer ersten Machbarkeitsuntersuchung gezeigt, dass eine minimalinvasive Behandlung eines Patienten mit schwerer Nasenscheidewanddeviation zu Änderungen in den berechneten Strömungsfeldern führte.

Weiterhin wurden Unterschiede in den Strömungsmustern gesunder Probanden und von Patienten, die unter einer Nasenatmungsbehinderung litten, identifiziert. Hierfür wurde die Atemströmung während der Ein- und Ausatmung von sechs Probanden und sieben Patienten berechnet. Um die individuell stark unterschiedlichen Geometrien und Strömungen miteinander vergleichen zu können, wurden die statischen Druck- und Wandschubspannungsinformationen an der Nasenscheidewand auf eine gemeinsame Schablone übertragen. Die Wandschubspannungsverteilungen der gesunden Probanden wiesen dabei deutliche Unterschiede während der Ein- und Ausatmung auf, welche bei der Patientengruppe nicht zu beobachten waren. Im Anschluss an diesen Machbarkeitsnachweis wurde sowohl das Patientenkollektiv auf jeweils 25 Patienten je Gruppe erweitert. Weiterhin wurde ein statistisches Formmodell der Nasenhöhle entwickelt, welches die Berücksichtigung der gesamten Nasenhöhle erlaubt. Die vorherigen Erkenntnisse konnten reproduziert werden. Weiterhin konnten Bereiche der Nasenhöhle identifiziert werden, in welchen Wandschubspannungsverteilungen beider Gruppen unterschiedlich sind. Die Bedeutung dieser Bereiche muss in weiteren Studien untersucht werden.

In einer letzten Untersuchung wurde versucht, die Simulation der Nasenatmung gegen den Goldstandard der funktionellen Diagnostik der Nasenatmung – der Rhinomanometrie – zu validieren. Hierfür wurde der Nasenatemwiderstand von drei Patienten mit unterschiedlich starker Obstruktion der Nase mittels Strömungssimulationen berechnet und mit in-vivo Messungen vergleichen. Es zeigte sich, dass die numerische Strömungssimulation den gemessenen Nasenatemwiderstand unterschätzt. Dieses Phänomen ist allen Publikationen, welche die numerische Strömungssimulation für die Berechnung des Nasenatemwiderstandes benutzen, gemein. Trotz intensiver Bemühungen konnte die Ursache dieser Unterschiede bislang nicht identifiziert werden.

1.2 Abstract

The prevalence of impaired nasal breathing is approx. 30 percent. Often, the cause of impaired nasal breathing is a perturbation of the airflow due to morphological changes within the nose. There is still no

generally accepted model allowing differentiation between healthy and disturbed nasal airflow. Existing measurement techniques only allow acquisition of integral measures (e.g. the nasal resistance). Findings of these methods cannot be easily correlated with the complex, tortuous anatomy of the nasal cavity.

Medical imaging enables a spatially resolved analysis of this complex anatomy. Knowledge of this anatomy allows calculation of patient-specific respiratory flow using image-based simulations. This approach allows the spatially and temporally resolved simulation of relevant parameters of nasal breathing.

This dissertation's focus was the development of a method based on simulations of nasal breathing allowing a statistical comparison of differences in nasal breathing between healthy subjects and patients. A first proof-of-concept study showed that minimally invasive treatment of a patient with nasal septum deviation, which led to an improvement in perceived nasal breathing, also led to changes in the calculated airflow.

Numerical flow simulation was used to identify differences in the flow patterns of healthy subjects and patients suffering from nasal obstruction. The patient-specific respiratory flow during inspiration and expiration of six subjects and seven patients was calculated. Static pressure and wall shear stress information on the nasal septum was transferred onto a common template in order to compare the heterogeneous individual geometries. Wall shear stress distributions of healthy subjects showed differences during inspiration and expiration, which could not be observed in the patient subgroup. The sample size of both groups was then extended to 25 patients each. Furthermore, a statistical shape model of the nasal cavity was developed allowing consideration of the whole nasal cavity. The previous findings could be reproduced using this approach. Additionally, areas could be identified, where wall shear stresses between subjects and patients differed. The relevance of these regions must be investigated in subsequent studies.

Additionally, another study aimed at validation of the simulation of nasal airflow using the current standard of functional diagnostic of nasal breathing. Here, the nasal resistance of three patients with different degrees of nasal obstruction was calculated and compared against in-vivo measurements. The simulations underestimated the in-vivo measurements. This is a common problem of all publications that reported numerically calculated nasal resistances. Despite intensive efforts, the cause of these differences has not yet been identified.

1.3 Introduction

Impairment of nasal breathing is commonly found throughout the whole population with a high prevalence of about 30 percent [1, 2]. Suffering from impaired nasal breathing often results in a severe limitation of quality of life. Typical sequelae of impaired nasal breathing are sleeping disorders, which might be as severe as sleep apnea, reduced performance during physical activities, work and school, as well as an increased proneness for headache and migraine [1, 3]. The causes for impaired nasal breathing are as manifold as these sequelae. Common causes are deformations of the nasal framework, as for example a deviation of the nasal septum, which can be of congenital or traumatic origin. Usually, impaired nasal breathing does not threaten a patient's life and only seldom causes acute pain for the patient. Nevertheless, the degree of suffering and the impact on the overall quality of life can be severe [3]. The relevance of impaired nasal breathing becomes even more evident by the number of surgical treatments performed each year. In 2015 approximately 150,000 operations targeting the lower nasal conchae and 100,000 operations targeting the nasal septum were performed in Germany alone. This equals almost two percent of all operations performed.

Even though there is a high social relevance of impaired nasal breathing, its diagnosis is still considerably limited. There is no method for a comprehensive, quantitative measurement of nasal airflow as of yet. Thus, it is difficult to reliably distinguish between impaired and healthy nasal breathing [2, 4, 5]. The current gold standard in functional assessment of nasal breathing is the rhinomanometry. This technique allows assessment of the nasal resistance of both sides of the nose by measuring the trans-nasal pressure drop as

well as the volume flow rate passing through the nose [6]. Studies on the diagnostic benefit of this technique are contradictory. While Vogt et al. [7, 8] reported good correlations between measurements of the nasal resistance using rhinomanometry and impaired nasal breathing, Bermüller et al. reported a high error rate [4]. Furthermore, the method only allows identification of impaired nasal breathing that is associated with a relevant increase of the nasal resistance. Diseases that alter the nasal airflow so that the inner milieu of the nasal cavity is disturbed without increasing the nasal resistance cannot be identified. A common example of such a disease is the Empty Nose Syndrome (ENS). Here, the nasal resistance is usually decreased, often due to a resection of the lower conchae, and the patient reports severe impairment of nasal breathing [8]. Another limitation of the rhinomanometry is that it only provides information on the nasal resistance as an integral measure for one side of the nose. No spatially resolved information is provided. Therefore, the location of the cause for an increased nasal resistance can only be identified using additional information, as for example gathered from medical imaging modalities as the computed tomography (CT).

The decision for a surgical intervention and the planning of this intervention is usually based on medical imaging techniques as CT or clinical investigations as the rhinoscopy and nasal endoscopy [9]. The rhinomanometry aims at replacing qualitative and subjective criteria with quantitative measurements, which would be an important step towards evidence-based medicine. While the rhinomanometry is used within clinical routine, its use is not mandatory [9-11]. Furthermore, its use is even discouraged in one clinical guideline regarding sleep apnea: "The application and results of this functional diagnostic are faulty and do not correlate reliably with a subjectively impaired nasal breathing." (translated to English from [10]). Due to the constraints of the rhinomanometry, the German Society of Oto-Rhino-Laryngology, Head and Neck Surgery defined the benefit of using rhinomanometric measurements as diagnostic tool before a surgical intervention as limited [9].

This situation regarding the pre-interventional functional diagnostical possibilities might be one cause for the overall unsatisfactory results of surgical interventions targeting the nose. Approximately 27 percent of all interventions do not lead to the targeted result, so that the patients still suffers from impaired nasal breathing [6, 12].

Therefore, a novel and robust method for functional assessment of nasal airflow might help to improve existing therapies and to avoid unnecessary interventions. In this cumulative dissertation thesis, the feasibility of numerical analysis of the patient-specific nasal airflow using computation fluid dynamics (CFD) is described. This technique (for details see section 1.4.3) allows the spatially and temporally high resolved calculation of nasal airflow. To allow this, a well resolved CT scan of the patient's nasal cavity is necessary. Except for the exposure to radiation during the CT imaging procedure, this approach is completely non-invasive.

The thesis is based on four academic, peer-reviewed publications, which describe different aspects of the numerical simulation of nasal airflow. The first publication entitled "*Numerical Flow Simulation – A Novel Method for Evaluation of Nasal Breathing*" (translated from the German original title "*Numerische Strömungssimulation – Eine neue Methode zur Beurteilung der Nasenatmung*.") focusses on describing the method of patient-specific nasal airflow simulation and its clinical applicability. Therefore, this work is described in the methods section of this synopsis. The other three publications focus on specific questions regarding the applicability of nasal airflow simulation for the diagnosis of impaired nasal breathing and the feasibility of patient-specific treatment planning using this method.

- S. Bessler, K: Mende, L. Goubergrits, J. Osman, T. Hildebrandt. *The Anterior Spreader Flap: A Minimally Invasive Alternative to the Auto Spreader Flap in the Treatment of Patients with Nasal Valve Dysfunction*. International Journal of Otorhinolaryngology and Head and Neck Surgery 2014, 3:184-189

Here, the aerodynamic effect of a surgical intervention was simulated using CFD to better understand the functional changes introduced due to morphologic changes.

- J. Bruening, L. Goubergrits, W. Heppt, S. Zachow, T. Hildebrandt. *Numerical Analysis of Nasal Breathing: A Pilot Study*. Facial Plast Surg 2017, 33:388-395

Here, a novel approach for statistical analysis of differences in aerodynamic parameters between healthy subjects and symptomatic patients was established revealing differences in wall shear stress patterns at the septal wall.

- J. Osman, F. Großmann, K. Brosien, U. Kertzscher, L. Goubergrits, T. Hildebrandt. *Assessment of nasal resistance using computational fluid dynamics*. Current Directions in Biomedical Engineering 2016, 2(1):617-621.

The aim of this study was to test, whether the nasal resistance, which is currently measured using rhinomanometry, can be assessed non-invasively using CFD.

These publications are described and summarized in detail in the results section of this synopsis.

1.4 Methods

1.4.1 Anatomy and Function of the Nose

In all publications this cumulative dissertation is based upon, images of air-filled volume of the nasal cavity are shown and discussed. Therefore, the anatomy of the nasal cavity will be explained briefly, to better introduce this intricate and tortuous geometry.

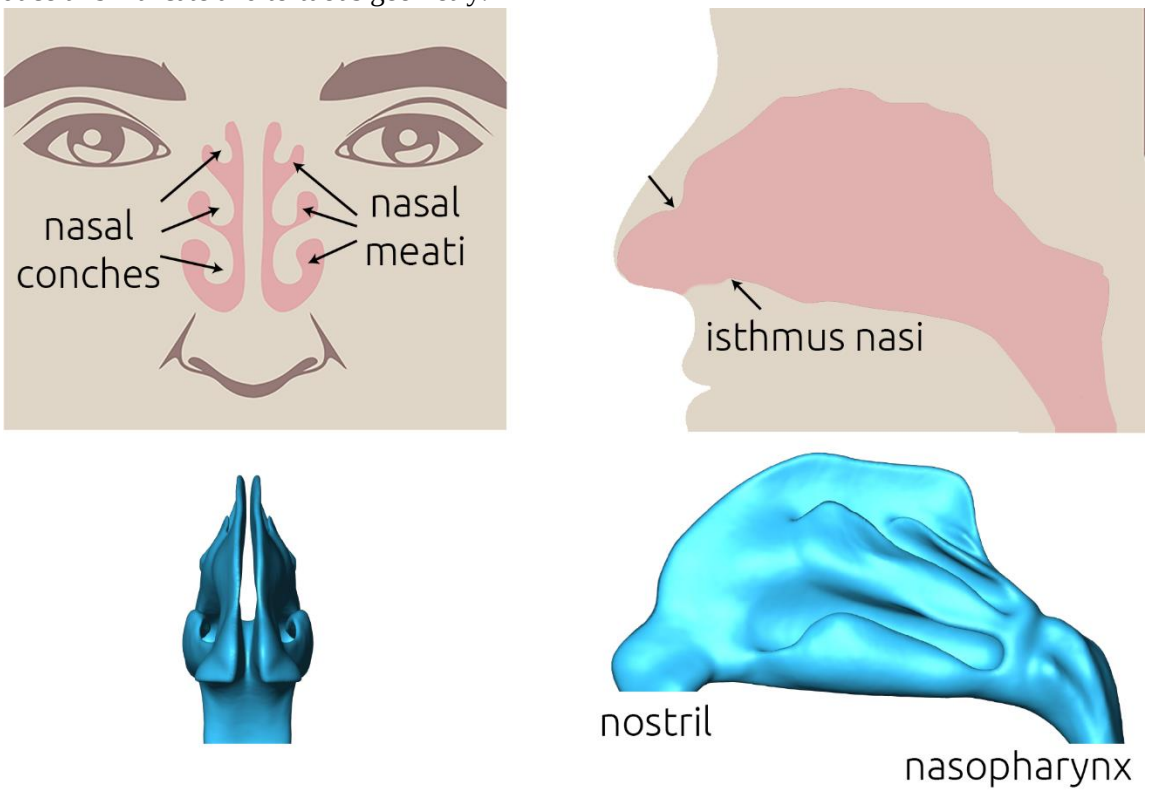

Figure 1: *Schematic visualization of the nasal cavity's geometry (upper panel). The nasal cavity has two symmetric sides. Three nasal conches at each side form the nasal meatus, giving the geometry of the nasal cavity its distinct and tortuous shape (edited from [14]). In the lower panel, an averaged three-dimensional geometry of the nasal cavity is shown from the front as well as from the side.*

The upper airways consist of the nasal cavity, the nasal sinuses and the ethmoidal air cells, which are connected with each other. The nasal cavity has two symmetric sides, which are separated by the nasal septum. The nostrils at the front of the outer nose connect the nasal cavity to the ambient, while it is connected to the airways via the nasopharynx. The nasal cavity as well as the nasal septum consist of cartilage as well as bone. On each side of the nose, there are three distinct, cylinder-shaped cartilage structures, the nasal conches. Below each nasal conch a tortuous cavity, the so-called nasal meatus, is formed [13]. A simplified visualization of the nasal cavity's anatomy is shown in figure 1.

The nose acts as passageway for exchange of air between the ambient and the lungs. Furthermore, particles within the inspired air are filtered by fine hair in the anterior part of the nose and the inspired air is moistened and temperated within the nose, protecting the delicate structures of the lungs. Within the olfactory region in the upper part of the nose, the sensory cells for the perception of smelling are located [13].

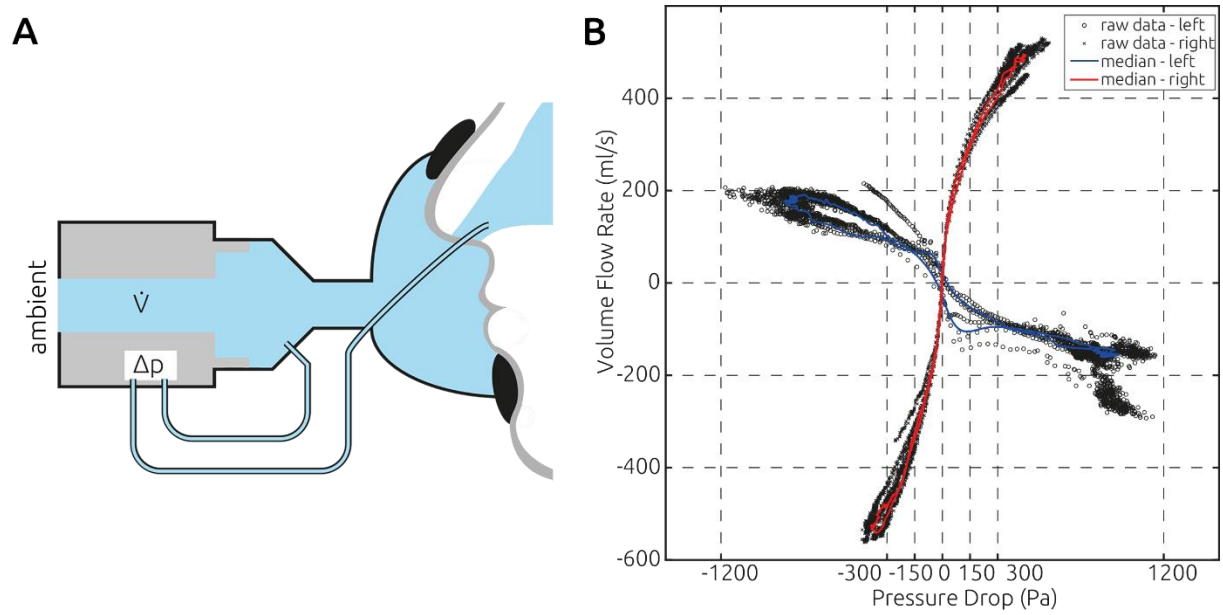

Figure 2: *A) Schematic representation of the measurement of nasal resistance using rhinomanometry. The patient is wearing a mask, to which a difference pressure sensor (Δp) and a volume flow probe ($\dot{V}$) are attached. One nostril is shut off using a plaster. The pressure difference across the open side of the nose is then measured using a tube that is inserted into the closed side of the nose and one tube that ends between mask and face [15]. B) Exemplary rhinomanometric measurement of a patient suffering from impaired nasal breathing. The raw data that was measured for both sides (black markers) of the nose is shown as well as the averaged curves (straight lines).*

1.4.2 Rhinomanometry

Since the rhinomanometry is the current gold standard of functional assessment of nasal breathing and it is important for understanding the research described later, its essentials will be described briefly.

The general setup of a rhinomanometric measurement is show in figure 2. During the measurement, the patient is wearing a mask. One nostril is shut using a plaster. A tube is pierced through this plaster, so that its opening lies within the nose. The contact between the plaster and tube has to be airtight. Using this tube, the static pressure at the height of the nasopharynx can be measured. A second tube is positioned within the mask, allowing measurement of the ambient static pressure. Both tubes are connected to a sensor measuring the pressure difference across the open side of the nose: $\Delta p = p_{ambient} - p_{nasopharynx}$. The patient is then asked to close the mouth firmly and to start breathing through the open side of the nose. The volume flow rate $\dot{V}$ passing through this side is measured using a respective probe in front of the mask. The mask has to be pressed tightly to the face, to avoid air passing between mask and facial skin. However, the mask must

not be pressed too tight, to avoid stretching of the facial tissue, which might alter the geometry of the outer nose. The lateral resistance of the open side of the nose is calculated from the quotient of the pressure difference and the volume flow rate: $R = \Delta p/\dot{V}$. This procedure is then repeated for the other side of the nose. The total nasal resistance is calculated using the formula for two parallel electric resistances: $R_{total} = 1/R_{left} + 1/R_{right}$. Therefore, the total resistance is always smaller than the smallest lateral resistance.

The general measurement principle is the same for all rhinomanometric devices available. However, details of the measurement might differ. In this study, the 4RHINO device (Rhinolab GmbH, Freiburg, Germany) was used. Here, the duration of one measurement is 20 seconds. The patient is asked to breathe quickly, to acquire a sufficient amount of breathing cycles within this time interval. This is necessary, because the measurement varies strongly between the different breathing cycles (see raw data in figure 2). Ideally, six or more breathing cycles are acquired, allowing calculation of a reliable mean curve [7]. This equals a slightly elevated breathing rate of 18 breaths per minute compared to approximately 12 breaths per minute during restful breathing. An exemplary result of a rhinomanometric measurement is shown in figure 2. Here, the volume flow rate is plotted against the pressure drop. Usually, the volume flow rates measured for the left side of the nose are inverted to allow better comparison of both curves. To illustrate the high variance during the measurements, the individual measurements are shown as well as the averaged curves.

Depending on the device used, different parameters are reported and used for diagnosis of impaired nasal breathing. However, a common criterium is the resistance at a specific pressure drop. Usually the so-called vertex resistance at a pressure drop of $\Delta p = 150$ Pa is reported. This resistance was shown correlate well with nasal obstruction [7]. Depending on the rhinomanometric device used, other parameters than the vertex resistance are evaluated as well and used for clinical diagnosis [16]. Some of those parameters are based on the typical hysteresis observed in rhinomanometric measurements (see figure 2). However, there is currently no general agreement on the cause of this hysteresis and intensive in-vitro experiments suggest, that this hysteresis is not associated with the nasal airflow but is an inherent aspect of the measurement technique used [17].

1.4.3 Simulation of Nasal Airflow Using Computational Fluid Dynamics

> **1. Publication:** T. Hildebrandt, J. Osman, L. Goubergrits. *Numerische Strömungssimulation –- Eine neue Methode zur Beurteilung der Nasenatmung*. HNO 2016, 64:611-618

Computational Fluid Dynamics (CFD) are a commonly used tool within the industry as well as in academic research. Theoretically, CFD can be applied to calculate any problem related to fluid dynamics. However, to correctly predict or calculate any flow using this technique, several aspects have to be considered. The most relevant aspect is, that the geometry or domain in which a flow is to be calculated has to be known. Due to the great advances in medical imaging within the last decades, spatially well-resolved three-dimensional information on different anatomical structures can be assessed using techniques as magnetic resonance imaging (MRI), computed tomography (CT) or echocardiography. This resulted wide use of CFD in clinical research. Here, its main application is the calculation of blood flow in different cardiovascular structures. In 2014, the first diagnostic tool based on numerical flow simulations was approved by the American Food and Drug Administration, moving the technique from clinical research to real clinical application (for further information see www.heartflow.com).

However, this method is not limited to simulation of blood flow within the human body, but can be used for every other fluid, as for example the brain's liquor or the air moving during respiration. One of the biggest promises of the numerical calculation of flow phenomena is, that it allows spatially and temporally well-resolved calculation of parameters that can only be measured at specific locations or in an averaged manner in-vivo. An example of this is the calculation of the pressure distribution in entire vascular networks, in

which measurements are only possible at specific locations, to which a catheter can be inserted for invasive pressure measurements. Another advantage of this method is, that it allows calculation of parameters for which no in-vivo measurement technique exists yet. Probably the most relevant example for such a parameter are the wall shear stresses. These shear stresses are a measure of the friction between a fluid and an adjacent, solid boundary. While some techniques for measuring wall shear stresses in-vitro exist, they cannot be measured in-vivo. In vascular and cardiovascular research, this parameter was found to be associated with remodeling processes of the endothelial layer as well as being correlated with the rupture risk of intracranial aneurysms [18]. Wall shear stresses are discussed to be relevant for the perception of nasal breathing as well, as they correlate with exchange of heat and moisture between fluid and tissue, both relevant aspects for the proper function of the upper airways [19, 20].

The simulation of any flow within the human body, be it air or blood, follows a common process pipeline composed of six subsequent steps: (1) image acquisition, (2) image segmentation, (3) describing the physical model, (4) discretization, (5) simulation, (6) analysis (see figure 3). These steps will be described in detail using the specific methods that were used in all four publications this thesis is based upon.

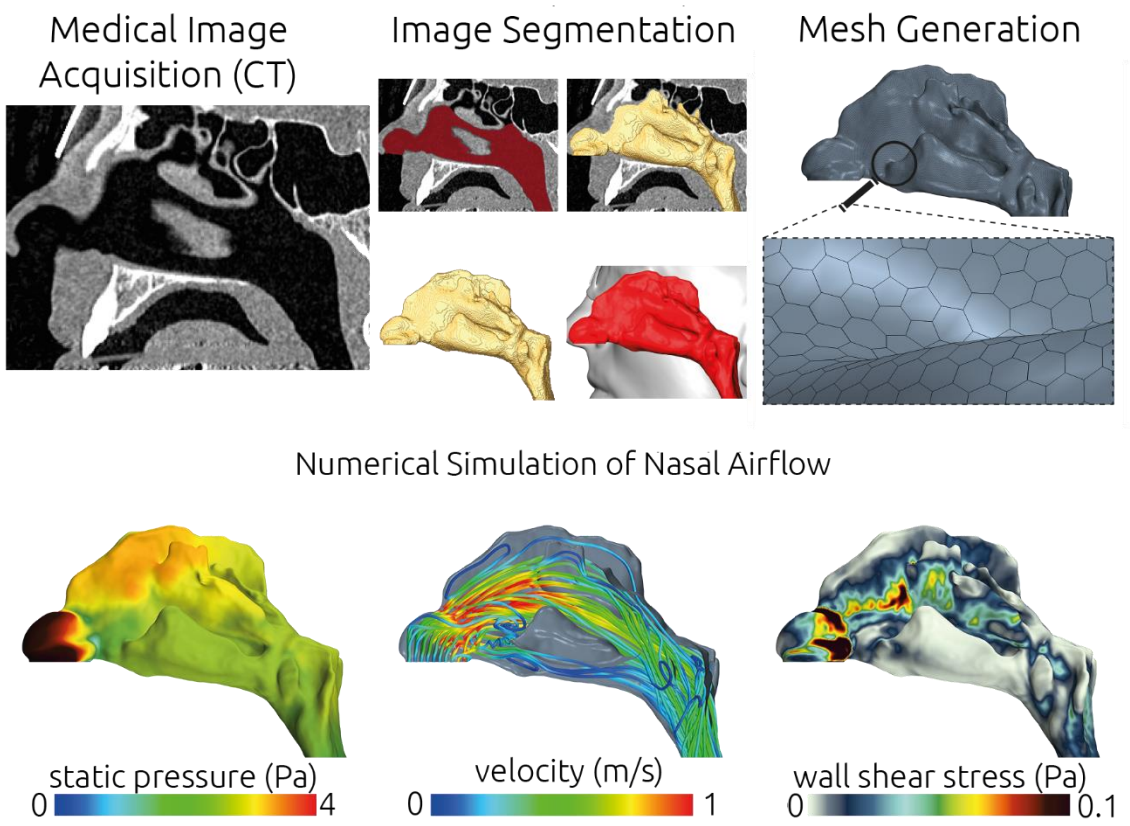

Figure 3: *Visual representation of the essential steps of the process pipeline for the numerical calculation of airflow in a patient-specific geometry of the nasal cavity. Medical images acquired using a CT scanner (upper left panel) have to be segmented. From this segmentation, a smooth, three-dimensional geometry of the nasal cavity is generated (upper middle panel). The final geometry is then discretized into a numerical mesh (upper right panel). Using appropriate boundary conditions, the airflow within the patient-specific geometry can then be calculated using CFD. In the lower panel the static pressure (left), the airflow velocity magnitude and orientation (middle) as well as the wall shear stresses (right) during inspiration are visualized.*

Image Acquisition and Image Segmentation: Theoretically, any spatially well resolved, three-dimensional imaging technique is suitable for reconstruction of the patient-specific geometry of the nasal cavity. However, CT images are currently the most reliable image-source, as they allow clear differentiation

between the air-filled nasal cavity and the surrounding tissue as cartilage, bones or mucus. This boundary between air and tissue is less clearly defined in other imaging techniques as for example MRI. In addition, the spatial resolution of CT is usually higher than that of MRI. As of yet, all studies using CFD for simulation of patient-specific nasal airflow relied on CT images for reconstruction of the nasal cavity's geometry [21, 22].

In this study, images were acquired using either a Sensation Cardiac 64 SIEMENS (Siemens AG, Germany) or a Toshiba Aquilion 64 scanner (Nasu, Japan) CT device. The reconstructed voxel size of the former device was $0.8 \times 0.25 \times 0.25\ \mathrm{mm}^3$, while the latter device provided an almost isotropic spatial resolution of $0.37 \times 0.37 \times 0.40\ \mathrm{mm}^3$. DICOM images generated by those devices were imported using the software ZIBAmira (v. 2015.28, Zuse Insitute Berlin, Berlin, Germany). These images were then segmented using level-set [23] and region-growing [24] algorithms implemented in ZIBamira. The Hounsfield (HU) threshold for the level-set methods was set to -250, meaning that image voxels with a Hounsfield value below or equal this threshold were considered candidates for the segmentation of the nasal cavity, while all other voxels belong to the tissue of the head. Even though semi-automatic methods were employed, intensive manual interaction was necessary for each segmentation. This manual interaction became necessary due to various reasons. First, the geometry of the nasal cavity is very tortuous, sometimes the narrow airways of the meatus are close to each other, causing artificial connections in the segmentation, which do not exist in the real anatomy. This is especially problematic if the nasal septum is skewed and artificial connections between both sides of the nasal cavity are created. Furthermore, the segmentation is to be limited to the three meatus of both sides of the nasal cavity. Neither the sinuses nor the ethmoidal air cells are included within the segmentation, since those large chambers are not relevant for the main nasal airflow and complicate evaluation of the computationally calculated nasal airflow.

After the segmentation is finished, a three-dimensional geometry of the nasal cavity is generated using a marching cubes algorithm [25]. This geometry is rough and edges resulting from the finite resolution of the CT images have to be smoothed. Since the Laplacian smoothing algorithm that was applied is not volume-preserving and can lead to shrinking of the geometry, the volumes of the original and smoothed geometry are compared. The volume change must not be larger than one percent. Afterwards, the smoothed geometry is truncated at both nostrils and the nasopharynx.

The physical model: The basic principle of any CFD simulation are the governing equations describing the behavior of viscous fluids. Those are the Navier-Stokes-Equations, non-linear partial differential equations describing the conservation of momentum, and the continuity equation describing the conservation of mass:

$$\rho\left(\frac{\partial \vec{u}}{\partial t} + \vec{u} \cdot \nabla \vec{u}\right) = \nabla p + \nu \cdot \nabla^2 \vec{u} + F$$

$$\nabla \vec{u} = 0$$

Here, $\vec{u}$ is the velocity vector, p is the static pressure, ρ is the fluid density and ν the kinematic viscosity of the fluid. The left side of the Navier-Stokes-Equations represent the spatial and temporal change of the fluid momentum. This change is driven by the righthand side of the equations. The pressure gradient (∇p) is a potential that can accelerate and decelerate the flow. The second term on the righthand side of the equations ($\nu \cdot \nabla^2 \vec{u}$) represents viscous effects and losses (e.g. friction). The last term on the righthand side (F) is a surrogate, describing all other possible forces that can act on a fluid as for example gravitational forces.

No general analytical solution of the Navier-Stokes-Equations exists as of yet. However, solutions of this set of equations can be calculated using various numerical methods. This process of numerical calculation of a solution of this set of equations is described as Computational Fluid Dynamics (CFD). The basic

principle of all methods for numerical solving of those equations is, that the region of interest, as for example the nasal cavity, must be represented as a set of small volumes or elements. This is the so-called numerical grid or mesh. A detailed description of the underlying principles and mathematics of the numerical calculation of fluid dynamics using the Finite-Volume-method, which was applied for all publications of this dissertation, is given in [26].

Discretization: As described previously, to numerically calculate the airflow within a model of the nasal cavity, this model must be separated into various finite volumes. This step, described as either mesh generation, pre-processing or discretization is essential for the following calculation of the solution. Obviously, the size of the finite volumes determines the spatial resolution of the solution. The finer the chosen element size, the higher the solution's resolution is. This, however, comes at the cost of an increase in the time necessary to calculate the simulation. Therefore, a good balance between the mesh resolution and the necessary computational time is necessary.

Furthermore, the mesh resolution itself might have an impact on the solution. Especially near the wall, a high resolution might be necessary to correctly model the interaction between fluid and the stationary wall. A mesh independency study is mandatory to identify which resolution is necessary to correctly calculate relevant airflow parameters. In such a mesh independency study the mesh resolution is increased step wise. The parameters that are to be investigated in the final CFD simulations are then calculated. Usually, the evaluated parameters should converge the finer the mesh resolution is. In this study, the pressure drop across the nasal cavity and the wall shear stresses are investigated. Therefore, those parameters were used to identify the necessary mesh resolution.

The following discretization was determined to provide mesh independent results. The average element edge length was 0.4 mm. Three layers of flat prism elements near the wall were used to correctly resolve the boundary layer at the walls. The growth ratio of these layers was set to 1.2, meaning that the second layer's thickness was 1.2 times as big as the first layer's thickness. The overall thickness of all three prism layers was set to 0.2 mm.

Simulation: In the beginning of this study, simulations were performed using ANSYS Fluent (ANSYS, Inc., USA). Later, this software was replaced by STAR-CCM+ (Siemens PLM Software, USA). Validation simulations using both programs to simulate airflow in the same geometries were performed to ensure that the software used had no impact on the results.

Analysis: Since this step varied due to different aspects investigated within the publications, the analysis performed in the individual publications is described in the corresponding section. This includes statistical methods used.

1.5 Results

In this section, the main results of the other three publications regarding the applicability of numerical simulations for diagnosis of impaired nasal breathing will be summarized briefly.

1.5.1 Proof-of-Concept of Therapy Planning Using Numerical Simulation of Nasal Airflow

> **2. Publication:** S. Bessler, K: Mende, L. Goubergrits, J. Osman, T. Hildebrandt. *The Anterior Spreader Flap: A Minimally Invasive Alternative to the Auto Spreader Flap in the Treatment of Patients with Nasal Valve Dysfunction*. International Journal of Otorhinolaryngology and Head and Neck Surgery 2014, 3:184-189

In this study, the case of a 36-year-old patient with severe septal deviation is reported. Despite previous surgical interventions, the patient reported bilaterally impaired nasal breathing. Due to previous

interventions, the patient refused another invasive surgical treatment of the deviated septum. Therefore, a minimally invasive procedure was performed, aiming at decreasing the airflow resistance induced by the bilateral narrowing of the anterior part of the nose. To facilitate this, a procedure called *Anterior Spreader Flap* (ASF) was performed. Here, only minor, endonasal alterations were performed. During a follow-up visit one year after the treatment, the patient reported a relevant improvement of his previously impaired breathing.

To better understand the effects the ASF procedure had on the nasal airflow, the pre-interventional as well as the post-interventional state of the patient-specific nasal cavity was reconstructed from medical imaging data. However, the post-operative CT scan only became available five months after the one-year follow-up visit due to an unrelated indication. As a CT scan is not indicated in a follow-up examination due to the exposure to ionizing radiation, this investigation only became available by chance. The inspiratory airflow was then simulated for both reconstructed geometries using the approach described previously (see section 1.4.3). Comparison of the pre- and post-interventional geometry revealed differences in the vicinity of the isthmus nasi. The pre-operative geometry featured distinct notches beginning at the isthmus nasi that were oriented into the intranasal region. These notches were almost completely removed after the ASF procedure, so that the transition between the upper, endonasal part and the internal part of the nose almost was rectangular. Even though the patient reported a relevant improvement of his nasal breathing, there was only a minor change in the transnasal pressure drop calculated before and after the intervention. While the pressure drop – and thus the nasal resistance – did decrease after the treatment, it is unclear, whether this relatively small change is responsible for the change in perceived nasal breathing. Besides the changes in the nasal resistance, the static pressure distribution within the nasal cavity did also change. After the treatment the spatial pressure gradient at the isthmus nasi is more distinct. Here, the color change and thus the pressure drop occurs across a straight line, while it is more diffuse in the pre-interventional simulation.

These results show that numerical simulation of airflow passing through the nasal cavity can provide additional information on the aerodynamic effects of different treatment modalities. This is especially helpful, since the tortuous geometry of the nasal cavity does not allow easy prediction of changes in the airflow caused by changes in the anatomy. In theory, this could also be used to perform a-priori investigations of different treatment modalities for one patient to identify the ideal treatment outcome. To facilitate this, the three-dimensional model of the nasal cavity could be altered similar to existing surgical procedures. The effect of this treatment can then be predicted numerically. While first studies describing this approach already exist [27, 28], they must be considered cautiously. There is currently no well-established model on what constitutes healthy airflow. Additionally, those studies as well as our own used the nasal resistance as means for comparison of the pre- and post-interventional state of the nasal airflow. However, recent findings suggest that the numerical calculation of the nasal resistance deviates strongly from in-vivo measurements (see section 1.5.3). Additionally, five months lay between the post-operative examination and the acquisition of the post-operative CT images. This further adds to these problems as additional changes in the patient's anatomy, for example due to inflammation or allergy, would have let to differences between the clinical and numerical examination.

1.5.2 Statistical Maps for Identification of Normal and Disturbed Nasal Airflow

> **3. Publication:** J. Bruening, L. Goubergrits, W. Heppt, S. Zachow, T. Hildebrandt. *Numerical Analysis of Nasal Breathing: A Pilot Study*. Facial Plast Surg 2017, 33:388-395

As described in the previous sections, calculation of the patient-specific inspiratory and expiratory airflow is possible when spatially well resolved image data of the patient-specific anatomy of the nasal cavity is available. Theoretically, this information on nasal airflow can be used for diagnosis and even treatment planning. However, no generally accepted definition of healthy nasal airflow exists yet [19]. While the

obstruction of the upper airways and the resulting increase of the total nasal resistance are a well understood cause for impaired nasal breathing, they are not sufficient to explain all problems of impaired breathing. Even though the nose is easily accessible, its tortuous geometry makes spatially resolved in-vivo measurements difficult. Numerical simulations could help to overcome this problem. First studies identified common flow features in healthy nasal airflow, as for example the inspiratory jet observed distally to the isthmus nasi [19, 29] or even found novel biomarkers correlating well with the NOSE scale as for example peak mucosal cooling [20]. However, another severe problem remains: the enormous heterogeneity of the upper airway's geometry.

Studies investigating differences between cohorts of patients and symptom-free subjects usually resort to qualitative comparison of flow features, reporting integral measures as the nasal resistance or try to compare similarly aligned coronal slices. Other approaches to unravel the tortuous geometry of the upper airways are the generation of average geometry of the healthy nasal cavity [30, 31] or unfolding of the complex 3D-geometry onto a rectangular 2D-plane [32]. All those approaches have the same limitation, they don't allow a spatial correlation between different geometries.

To overcome this problem, an approach developed for the numerical analysis of intracranial aneurysms was employed for the nasal cavity [18]. Here, a simplified template of the nasal cavity's septal wall was generated from measurements of 13 patients (6 symptom-free, 7 reporting impaired nasal breathing). This grouping was based on the patient's self-perception as well as an examination by an ENT-specialist focusing on rhinology. Only patients that did not report any impairment of nasal breathing were considered for the healthy control group, whereas ambiguous answers led to exclusion. The patients' self-assessment of being symptom-free was confirmed by rhinoscopic or endoscopic investigation of the nasal cavity, palpation of the nasal structure as well as the CT images. However, no patient had to be excluded from the group of symptom-free subjects. CT images in the symptom-free group were indicated by a variety of symptoms, such as facial pain, hyposmia or anosmia, unilateral swelling of an eyelid, possible cerebrospinal fluid leak, recurrent epistaxis and epiphora.

The patient-specific nasal airflow during inspiration and expiration was calculated for all 13 patients. For each patient, the septal-wall geometry of the left and right nasal cavity was separated, respectively. Those individual septal wall geometries were then aligned with the simplified template, to create a spatial correlation between the individual geometries. Finally, wall shear stress and static pressure information at the septal wall were interpolated onto the simplified template using a linear interpolation algorithm. Thus, flow information of all patients was transformed onto the same geometry, allowing a spatial comparison of flow features, since the same anatomical landmarks were mapped onto the same region of the template.

This approach allowed statistical comparison of spatial distributions of static pressure and wall shear stresses between symptom-free and symptomatic cases. Firstly, the sample-averaged distributions revealed the same flow phenomena which are typical for restful nasal breathing. During inspiration, the main flow resistance is induced at the isthmus nasi, which can be visualized by means of the pressure distribution at the septal wall. Here, a clear pressure difference between the anterior part of the nose and the nasal cavity can be observed. During expiration, the pressure is declining more homogenously from the anterior parts of the nasal cavity toward the nostrils. The nozzle effect of the isthmus nasi is visualized by the averaged wall shear stress distributions during inspiration. Here, high wall shear stresses are present distally to the isthmus nasi and reaching into the middle meatus. This is caused by the so-called inspiratory jet, which is formed at the isthmus nasi and is directed towards the septal wall and the middle meatus. These findings indicate that the averaging of the patient-specific distributions resulted in a plausible distribution of averaged static pressure and wall shear stress values.

In the symptomatic subgroup, the wall shear stress distribution during inspiration did not reveal a band of high values within the middle meatus. For this group, the wall shear stress distributions during inspiration and expiration were similar, indicating similar flow patterns within the vicinity of the wall during inspiration and expiration. However, whether this similarity of wall shear stress distributions during inspiration and expiration are a good predictor for the perception of impaired nasal breathing must be investigated in a prospective study with a larger sample size. Nonetheless, this study was, at least to our best knowledge, the first investigation revealing differences in numerically calculated flow patterns between healthy subjects and patients suffering from impaired nasal breathing, where both groups were distinguished solely using the subjective patient perception.

1.5.3 In-Vivo Measurement vs. In-Silico Calculation of the Nasal Resistance

> **4. Publication:** J. Osman, F. Großmann, K. Brosien, U. Kertzscher, L. Goubergrits, T. Hildebrandt. *Assessment of nasal resistance using computational fluid dynamics*. Current Directions in Biomedical Engineering 2016, 2(1):617-621.

Even if the benefit of rhinomanometric measurements is controversial, this method is the current gold standard of functional assessment of nasal breathing. The nasal resistance calculated using this technique correlates well with impaired nasal breathing [7]. If the numerical simulation of nasal airflow is to support or even replace those measurements, it must be validated against this current gold standard. Interestingly, no such validation study is to be found within academic literature. While several studies report resistances measured using rhinomanometry, as well as calculated using numerical simulations [19, 27], no extensive discussion of those values exists yet. In one study by Zhao et al., a poor but significant correlation between the in-vivo measured nasal resistance and the in-silico calculated resistance for the same geometries was reported ($r = 0.41$) [20]. Subsequently, Garcia et al. questioned the origin of this poor correlation in a letter to the editor [33]. In their reply Zhao et al. stated, that the low correlation was to be expected, since the study design did not aim at comparing both techniques [34].

Therefore, we performed an experiment to determine, whether nasal resistances measured in-vivo using rhinomanometry could be calculated in-silico as well. Data of three patients, one with no nasal obstruction, one with a mild obstruction and one with a severe obstruction, was used to incorporate the wide range of resistances observed within clinical routine. For those three patients well resolved CT-images as well as rhinomanometric measurements were available retrospectively. The rhinomanometric measurements were performed using the 4RHINO system (Rhinolab GmbH, Freiburg, Germany). Each measurement consisted of at least 5 breathing cycles. The patient-specific geometries of the nasal cavity were reconstructed using the approach described in section 1.4.3.

The lateral resistance as well as the total nasal resistance are not constant values. They are functions of the pressure drop across the nasal cavity and the flow rate passing through the nose. Therefore, the resistance at a specific pressure drop, the so-called vertex resistance, is commonly used to describe the patency of the nose. In case of the device used, the vertex resistance at a pressure drop of $\Delta p = 150$ Pa is recommended. Therefore, the resistance at this pressure drop for both sides of the nose was measured during inspiration and expiration. Unfortunately, for one patient the exported files containing the measurements of the right side were corrupted. From this resistances, the corresponding flow rates were calculated: $\dot{V} = \Delta p / R = 150\ \mathrm{Pa}/R$. This flow rate was then used as boundary condition for the numerical flow simulations. Ideally, the simulations would result in the same pressure drop and thus the same lateral flow resistances as measured in-vivo.

However, the differences of the resistances calculated using CFD and those measured in-vivo were enormous. While the measured resistances varied between $R = 0.31\ \mathrm{Pa \cdot s/ml}$ and $R = 5.35\ \mathrm{Pa \cdot s/ml}$, the

numerically calculated values were one to two orders of magnitude lower. Thus, the numerical simulations grossly underestimated the values measured in-vivo. Interestingly, the values measured using rhinomanometry agreed well with those from large multi-centric studies [7], indicating that those measurements are at least plausible. Furthermore, the numerically calculated values agree well with those values reported in other studies, that reported numerically calculated nasal resistances. In a review paper, Kim et al. reported, that numerically calculated values usually are below $R = 0.05\ \mathrm{Pa \cdot s/ml}$ [22]. Even in simulations of patients with severe nasal obstruction, calculated resistances are below $R = 0.2\ \mathrm{Pa \cdot s/ml}$ and thus significantly below values to be expected from in-vivo measurements [28, 35].

While the first assumption might be, that numerical simulation of nasal airflow is not suitable to correctly calculate the nasal resistance, several in-vitro experiments have been performed, revealing good agreements between numerical calculated flow fields and those measured in-vitro [36]. Furthermore, all assumptions made during the simulation of nasal airflow are thoroughly tested and well understood and agreed upon. As of yet, it is completely unknown what is the cause for these gross differences between the nasal resistances obtained using both methods. During the first conference of the newly established *Society for Computational Fluid Dynamics of the Nose and Airway* (SCONA, www.scona.org) these findings were a well-discussed topic. However, the answer on the cause of this problem remains elusive.

1.5.4 A Statistical Shape Model of the Nasal Cavity – Proof of Concept and Standardization

Published in: J. Bruening, T. Hildebrandt, W. Heppt, N. Schmidt, H. Lamecker, A. Zengel, N. Amiridze, H. Ramm, M. Bindernagel, S. Zachow, L. Goubergrits,. *Characterization of the Airflow within an Average Geometry of the Healthy Human Nasal Cavity*. Nature Scientific Reports 2020, 10(1):3755.

In section 1.5.2 an approach allowing comparison and statistical analysis of different patient-specific geometries was presented. Here, aerodynamic information at the septal wall could be transferred onto a simplified stencil of the nasal septal wall. While this approach allows spatial correlation of different geometries, it has two major limitations as described in detail in the corresponding publication. First, the approach is limited to the septal wall. Neither wall-bound aerodynamic information within the meatus nor information that is only defined in the volume, as for example the velocity, can be analyzed using this method. The second limitation is, that it only provides a spatial correspondence but no semantic correspondence. This means, that anatomical structures such as the olfactory cleft or the isthmus nasi will be represented at the same spatial location of the simplified template. However, the elongation of those regions on the template might vary due to their differing sizes in the patient-specific geometries. Finally, although this is no limitation of the method used but of the study design, the study was based on a very small number of samples. Only 6 and 7 patients were investigated in the respective groups.

To overcome this problem, a so-called statistical shape model (SSM) of the healthy nasal cavity was developed. An SSM is created by identification of common anatomical structures in a set of geometries. Here, the relevant anatomical structures were the septal wall, the outer nose, the isthmus nasi and the inferior, middle and superior meatus. These regions were identified in a set of 25 geometries of symptom-free subjects. Here, the definition of being symptom-free was the same as in the study presented in section 1.5.2, meaning that neither the patient reported any impairment of nasal breathing nor examination by an ENT-specialist revealed pathological alterations of the nasal cavity's anatomy.

The SSM is then a representation of those geometries, and allows identification of different geometric modes, which are responsible for the shape of the anatomy [39, 40]. Lamecker et al. described the generation of statistical shape models in detail [41-43].

Using an SSM has several advantages compared to other methods previously described. First, it allows the generation of a mean geometry of the nasal cavity of symptom-free subjects. This geometry is an average

of all 25 patient-specific geometries that have been used for the generation of the SSM. There is an enormous interest in a standardized geometry of the nasal cavity, especially for investigations regarding the deposition and distribution of particles of pharmaceuticals within the upper airways. Those studies are currently performed using individual geometries [44-46]. Existing approaches to generate an average geometry of the healthy nasal cavity were performed without any semantic correlation between the geometries. One geometry, which was generated by averaging commonly aligned CT data sets, features a rough surface and non-physiologic topology [31]. Gambaruto et al. used a more sophisticated approach for generation of an average nasal cavity that resulted in a plausible geometry [30]. However, only three geometries were averaged in this study and the final geometry was not made publicly available.

Therefore, the question whether the average geometry of the nasal cavity of symptom-free subjects might be used as generalized model was addressed first. This question was also used as proof-of-concept study to determine, whether a spatially resolved comparison of wall-bound flow information was feasible using the SSM. A standardized geometry might be of utmost interest for investigations regarding the nasal cavity. However, note, that the non-linear relationship between the nasal cavity's shape and the airflow within the nasal cavity, which is described by the Navier Stokes Equations, does not allow the assumption that an average airflow will be found within the geometric average.

Airflow within the 25 symptom-free subjects used for generation of the SSM was calculated as well as the airflow within the average geometry (see Figure 4a). As all geometries within the SSM not only feature the same semantic regions but also the exact same triangulation of the surface, a point-wise comparison of wall-bound flow parameters became feasible. Using this approach, the wall shear stress and static pressure distributions during inspiration and expiration were compared between the average geometry and the distribution calculated for the 25 symptom-free subjects. Additionally, several integral measures were calculated: uni-lateral and total nasal resistance, averages and maximum values of wall shear stresses and velocities, the ratio of the airflow passing through the left and right nasal cavity (flow imbalance). Also, the minimal cross-sectional area of the nasal cavity was calculated and compared.

Relevant deviations were observed regarding the integral measures. For all parameters, the value calculated for the average geometry lay below the median of the values calculated for all 25 symptom-free subjects (see Figure 4a). For all parameters, except the average airflow velocity and the flow partitioning, the value calculated for the average geometry also lay below the 25-percent quantile of the healthy subjects' distributions. However, there were also lower values observed in those distributions. According to a Shapiro-Wilk test, the underlying distributions of all parameters were normally distributed except for the lateral and total nasal resistance. Due to this inconclusive statement regarding normality, a Kruskal Wallis test was used to determine whether the average of the distributions differed significantly from the respective value calculated for the average geometry. No significant deviations were observed for any distribution using a significance level of 0.05. Even though the test suggests no significant deviation, its findings must be considered cautiously. To definitely answer the question whether the observed deviations are significant or not, an equivalence tests and larger sample sizes would be warranted.

To determine, whether the observed deviations were caused by geometric differences between the average geometry and the individual geometry, the cross-sectional area was calculated for different positions along the length of the nasal cavity from nostril to choane (see Figure 4b) using a method described by Garcia et al. [47]. Here, the median of the individual distributions was close to the value calculated for the average geometry for the anterior half of the nasal cavity. In the posterior half, the cross-sectional area of the average geometry was slightly larger than the median of the individual geometries. However, the minimal cross-sectional area, which is usually found in the isthmus nasi, was also larger in the average geometry compared to the individual geometries. No significant deviation was observed for either the minimal cross-sectional area or the cross-sectional areas along the length of the nasal cavity. As the minimal cross-sectional area is

strongly correlated with the nasal resistance [47], this might be part of the reason, that the average geometry features a smaller resistance than most individual geometries. However, as the definition of the cross-sectional area used in this study is based on aerodynamic simulations (i.e. the cross-sections are perpendicular the streamlines of the airflow) there also might be an interaction of the altered flow towards the calculation of the minimal cross-sectional area.

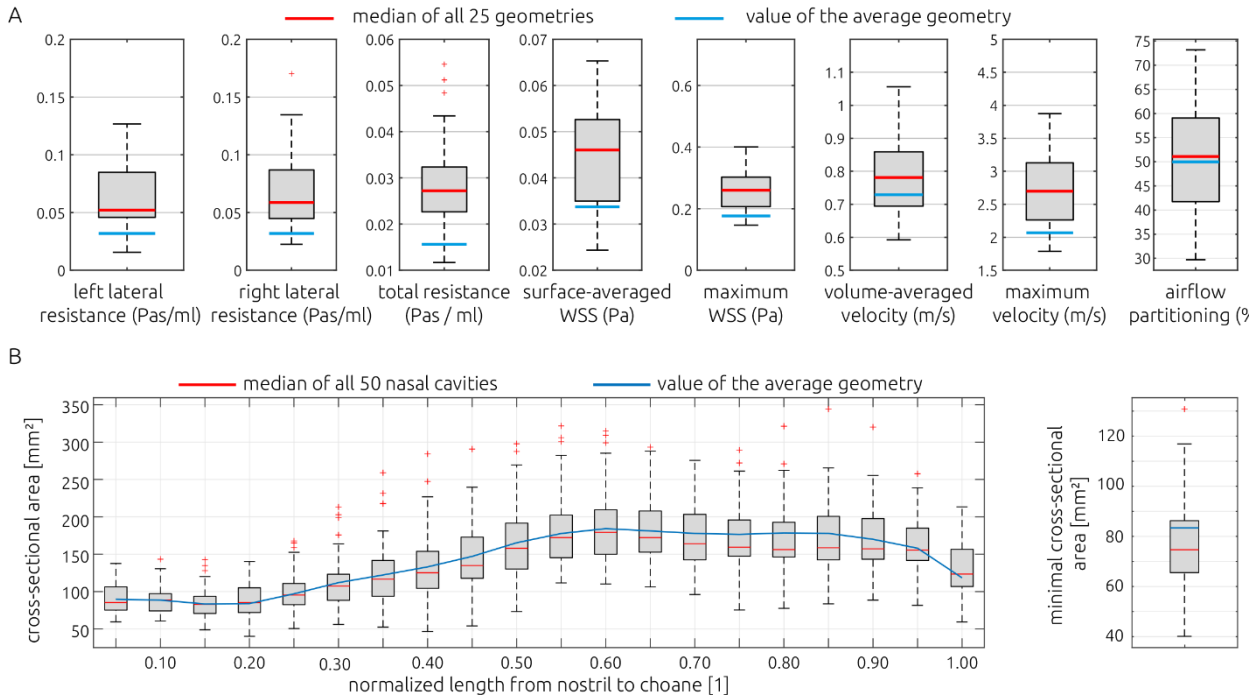

Figure 4: *a) Comparison of the integral measures calculated for the 25 symptom-free subjects and the average geometry. The distributions calculated for the 25 subjects are shown as boxplots, where the box represents the range from the 25 to the 75 percent quantile. The respective distributions median is indicated by a red bar, whereas the value calculated for the average geometry is indicated using a blue bar. b) The same visualization is used to show the cross-sectional area for different positions along the length from the nostril to choane. Also, the minimal cross-sectional area is shown. Both figures are adapted from Bruening et al. [48].*

Finally, a spatially resolved comparison of the wall shear stress and static pressure distributions calculated for the average geometry and the 25 symptom-free subjects was performed. Here, the advantage of the SSM becomes evident: All individual distributions could be mapped onto the same geometry, allowing calculation of averages, deviations and other descriptive parameters as well as point-wise statistical comparison.

Figure 5a shows the wall shear stress distributions during inspiration that were calculated for the average geometry as well as the mean and standard deviation of the distributions calculated for the symptom-free subjects. In general, the location of areas featuring relatively high wall shear stresses above 0.1 Pa correlate well between the average geometry and the mean of the 25 symptom free subjects. However, the area affected by those wall shear stress levels seems to be smaller in the average geometry. This is also quantified by the surface histogram shown in Figure 5b. Here, the percentage of the surface area of the symptom-free subjects' nasal cavity, which is affected by a respective wall shear stress range, is visualized using box plots. The value for the average geometry is shown using a blue line. The area percentage of the average geometry affected by small wall shear stress magnitudes is larger than that of the symptom-free subjects. This agrees well with the observation regarding the integral measures of wall shear stress shown in Figure 4.

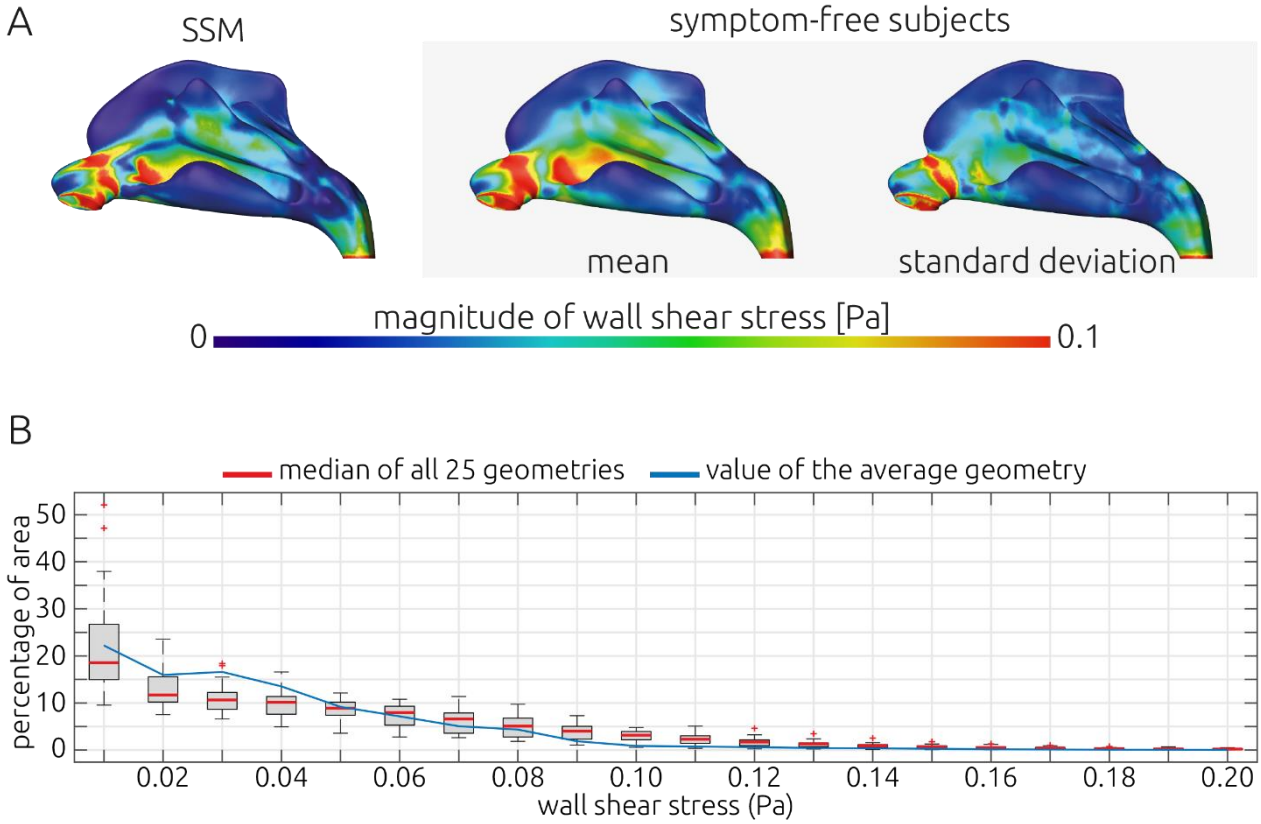

Figure 5: A*) Visualization of the wall shear stress distribution calculated for the average geometry (left) as well as the mean and standard deviation of the distributions calculated for the 25 symptom-free subjects. B) Surface histogram of calculated wall shear stress distributions. For each bin of the histogram the percentage of the surface area that is affected by this wall shear stress magnitude is presented using box plots for the 25 symptom-free subjects and a single value (blue line) for the average geometry. Both panels are adapted from Bruening et al. [48].*

While the airflow calculated within the average geometry of the nasal cavity did not match the average of the individual geometries in every detail, the parameters calculated also did not differ grossly. The average geometry of the nasal cavity was more regular, smoother and, most importantly, perfectly symmetric. It might be considered as an idealized state of the healthy nasal cavity but not as an average. As the geometry is plausible and features all common geometric landmarks such as the three meatus and a distinct isthmus nasi and the flow also features commonly observed patterns such as the inspiratory jet, resulting in a flow concentration in the vicinity of the middle meatus, the average geometry as well as all data of this study was made openly available. While the findings were not entirely conclusive, we cautiously advised using the geometry as a substitute for individual geometries in studies were only a single individuum is investigated. While the geometry might not be generating a perfect average of healthy nasal airflow, the same is true for individual healthy geometries and the advantages of comparability and reproducibility of using a freely available geometry might outweigh those uncertainties.

1.5.5 Statistical Comparison Between Healthy Subjects and Patients Using the Statistical Shape Model

As the previous study had shown, that using an SSM is a viable method for comparison of wall-bound information of different subjects, the method was applied to 25 patients with severe septal deviation, which caused impairment of nasal breathing. For those 25 geometries spatially resolved distributions of wall shear stress were mapped using the SSM. Those distributions and the same integral parameters as described in Bruening et al. [48] and Figure 4B were analyzed.

The integral parameters' distributions are visualized in Figure 6 using box plots. Here, the distribution calculated for the patients suffering from impaired nasal breathing are represented by the left box plot, whereas the symptom-free subjects' distributions are represented by the right box plot. No significant differences between both distributions were found for any integral parameter, except for the average velocity, according to a Kruskal Wallis test using a significance level of p = 0.05. The average velocity calculated for the symptom-free subjects was slightly larger than that of the patient group ($u_{avg,healthy} = 0.78\ vs.\ u_{avg,impaired} = 0.71\ , p = 0.03$). No significant deviation was found for the lateral and total resistance. However, the resistances calculated for the symptom-free subjects featured a larger variance. The minimal cross-sectional area calculated for the patient group also featured a larger variance, reflecting the asymmetry resulting from the septal deviation.

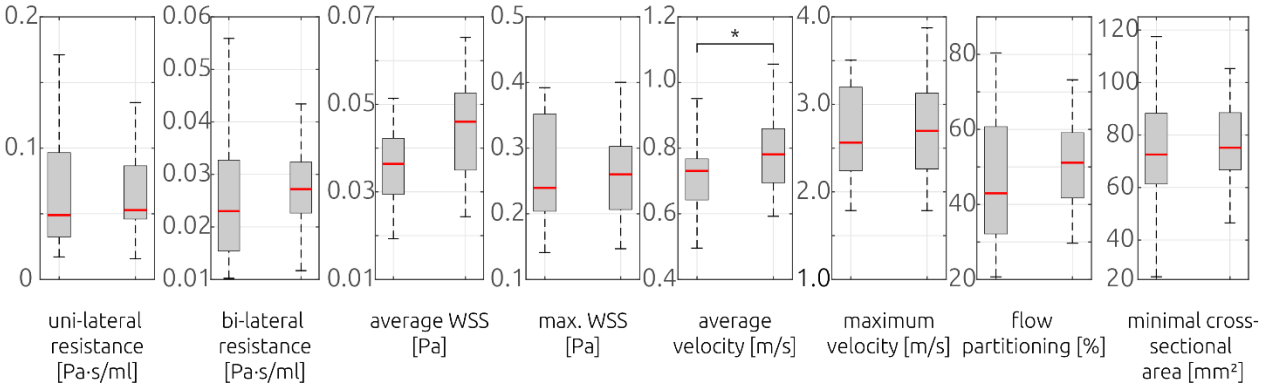

Figure 6: Box plots comparing the distributions of different integral parameters for the patient (left box plot) and healthy subject group (right box plot). Only for the average velocity a significant deviation between both groups was identified.

In 13 of 25 patients the left nasal cavity featured the larger obstruction. Before a spatial resolved statistical analysis was performed, the asymmetry caused by the septal deviation had to be accounted for. Here, the patient geometries were mirrored to ensure that the more obstructed side was always on the left. Otherwise, averaging of the distributions might mask the effects of the septal deviation. Afterwards, a Kruskal Wallis test was used to identify regions within the nasal cavity, where the calculated distributions of wall shear stresses differed significantly. To facilitate this, the hypothesis test was evaluated for each vertex of the triangulated surface. However, a stricter significance level of p = 0.001 was chosen, to account for accumulation of alpha errors. The results are shown in Figure 7. Here, the distributions of the mean wall shear stress distribution in the left and right nasal cavity are shown for both groups as well as during inspiration and expiration. Areas where the Kruskal Wallis test suggested significant deviations are highlighted in red.

In general, the agreements in the wall shear stress distributions on the least obstructed side in the patients (right) and the symptom-free subjects are minimal. During inspiration, a distinct band of high wall shear stresses is observed, reaching from the isthmus nasi towards the middle meatus. During expiration, the wall shear stress magnitudes are smaller and only in the vicinity of the isthmus nasi, high wall shear stresses are observed. This good agreement is also supported by the visualization of areas featuring significant differences. Here, only small regions are highlighted.

In contrast, there are distinct differences in the wall shear stress distributions of both groups during inspiration as well as expiration. In general, the wall shear stress distributions calculated for the obstructed side (left) in the patient group during inspiration and expiration are strikingly similar. There is a large patch of high wall shear stresses in the vicinity of the isthmus nasi. This agrees well with the earlier findings presented in section 1.5.2. The distinct narrow band of high wall shear stresses, that reaches from the isthmus nasi towards the middle meatus during inspiration in the symptom-free subjects, is only observable in the

least obstructed side for the patient group. This indicates that the inspiratory jet that is usually formed during inspiration [29], which impinges on the septal wall resulting in a distinct shear layer and therefore higher wall shear stresses, is less prominent in the obstructed side in the patient group.

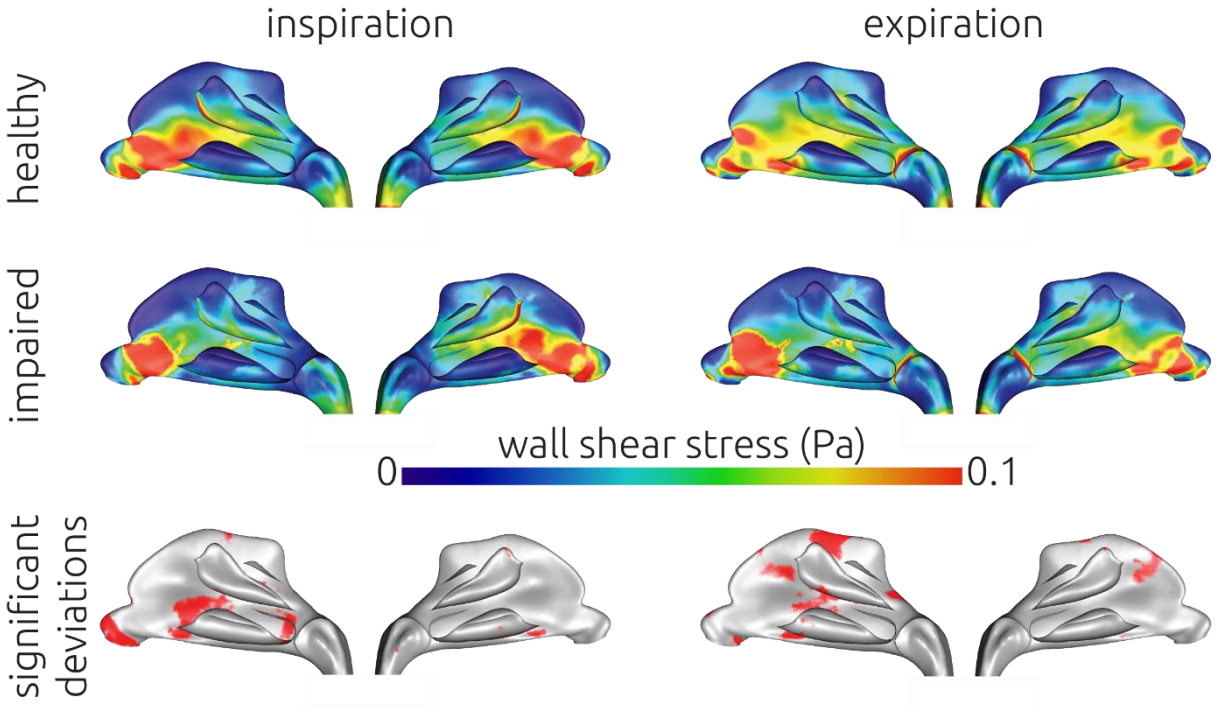

Figure 7: *Visualization of the mean wall shear stress distributions calculated for the 25 symptom-free subjects (upper row) and the 25 patients reporting impaired nasal breathing (middle row). Distributions are presented for the inspiratory (left) and expiratory (right) phase. In the lower row, areas where a statistic significant difference between both groups was identified using a Kruskal Wallis test ($p < 0.001$) are highlighted in red. All individual geometries of the symptomatic patients were mirrored to ensure, that the obstructed nasal cavity lay always on the left side.*

Several regions featuring a significant difference between the wall shear stress distributions calculated for both groups were identified for the obstructed side of the nasal cavity. During inspiration, the largest connected area observed was found at the septal wall in between the middle and lower meatus. Also, a small region near to the choane and the inflow surrounding the nostril were identified. During expiration, significant differences were also found at the septal wall between the meatus. However, here the largest region is found at the superior end of the nasal cavity, where the olfactory cleft is located.

1.6 Discussion and Outlook

The findings of this thesis suggest that numerical simulation of nasal airflow in combination with the application of statistical shape models allow statistical analysis and comparison of spatially resolved aerodynamic parameters in the nasal cavity. This combination of tools is promising for a better understanding of the complex flow within the upper airways. It provides spatially and temporally well-resolved information on the nasal airflow. Furthermore, its application already was fundamentally responsible for the identification of common flow phenomena, such as the inspiratory jet formed by the isthmus nasi or the large stationary vortex forming in the anterior part of the nose [29].

1.6.1 Discussion of the Presented Approach for Statistical Comparison of Spatially Resolved Aerodynamic Information

In a proof-of-concept study we were able to demonstrate, that a point-wise comparison of the spatially resolved flow information allows identification if differences in wall shear stress patterns between symptom-free subjects and symptomatic patients. However, in this study only a small sample sizes were used. Furthermore, the method used for mapping of individual wall shear stress distributions still had major limitations. The mapping onto the simplified stencil of the septal wall only allowed comparing similar regions at the septal wall. And even here, the mapping only followed a linear interpolation scheme. Nonetheless, using this approach, we were able to identify first differences in the respective wall shear stress maps. Most prominently, the wall shear stress maps calculated for the symptomatic patients were more similar during inspiration and expiration than that of the symptom-free subjects.

To overcome those limitations as well as to provide a standardized geometry for investigation of nasal airflow, a statistical shape model was developed using 25 symptom-free subjects [48]. In contrast to the simplified stencil used in the proof-of-concept study [second publication], the average geometry generated using the statistical shape model is the exact statistical average of all 25 geometries. While the definition of the statistical shape model still required manual interaction, the identification of all shape modes and their respective weights is performed using a principle component analysis allowing a robust and reproducible representation. Using this approach, the initial findings of the proof-of-concept study could be replicated. The average wall shear stress distributions calculated for 25 symptom-free subjects and 25 symptomatic patients during expiration and inspiration were compared. First, the distributions calculated for the symptomatic patients were strikingly similar during inspiration and expiration. Second, different regions within the nasal cavity featuring significant differences between the symptom-free subjects and symptomatic patients were identified.

However, the importance of those regions has yet to be investigated. One region, located at the septal wall close to the tip of the middle concha, agrees well to the location of the region featuring peak-mucosal cooling, for which Zhao et al. found a good correlation with impaired nasal breathing [20]. The relatively large region at the nostril of the most obstructed nasal cavity is most likely an artifact due to the boundary conditions chosen. Taylor et al. discussed that the wall shear stress at the beginning of the outer nose must be considered cautiously, when the ambient surrounding the nose is not included within the simulation [29]. During expiration, wall shear stresses in the symptomatic patient group were significantly lower in the vicinity of the olfactory cleft compared to the symptom-free subject group. Again, whether this difference might be a reason for perception of impaired nasal breathing is yet to be investigated. As the olfactory cleft and the airflow within the olfactory cleft are essential for the sense of smell as well as taste, it seems warranted to further investigate these findings.

On the least obstructed side of the nose, almost no regions featuring significant differences were observed. This is interesting, as all symptomatic patients suffered from septal deviation. This condition usually affects both sides of the nose, as it results in an overly asymmetric anatomy. However, the airflow, at least the airflow close to the wall, was similar for the symptom-free subjects and the symptomatic patients. It might be hypothesized that the autoregulation of the nasal cavity's width and thus the airflow on this size allows to compensate anatomical variations caused by the septal deviation. While the more obstructed side of the nose is too narrow, a potentially too wide passageway can be reduced by swelling of the nasal conches and in the Kiesselbach area [51].

While it is still unclear, whether or how the regions that were identified using the presented approach correlate with perception of impaired nasal breathing, the statistical comparison of spatially resolved parameters that were calculated using computational fluid dynamics was successfully demonstrated. While

these findings are promising, some limitations must be considered and there are questions that are yet to be answered.

First, larger sample sizes are warranted to further increase the robustness of the approach. While, at least to the best of our knowledge, no numerical studies featuring a sample size of more than 25 symptom-free subjects and 25 symptomatic subjects exist [19, 20, 49, 50], traditional clinical studies using established techniques as for example acoustic rhinometry or rhinomanometry often allow for larger sample sizes [7]. Therefore, the cohorts for the symptom-free subjects as well as the symptomatic patients will be increased in future studies. As currently all symptomatic patients featured a severe deviation of the nasal septum extension by other pathologies is warranted. Increasing the sample size can also improve the robustness of the statistical shape model, as shape modes that better explain the overall shape variance might be identified [41,42]. However, another statistical shape model of the nasal cavity presented by Keustermans et al., which was generated using 46 symptomatic geometries, did require more than 46 shape modes to account for 95 percent of the shape variance [52]. The same shape variance observed in the shape model presented in this thesis is explained by 33 shape modes. While additional geometries might even reduce this number further, this comparison also suggests, that the model performs comparable to other models.

Regarding the limitations of the presented method, the most relevant one is the underprediction the trans-nasal pressure drop compared to the current gold-standard technique of rhinomanometry. As shown in the fourth publication of this thesis [15], there is no agreement between the numerically calculated and the rhinomanometric measured nasal resistance. The question was and still is: What is the cause of this significant difference?

1.6.2 Causes for Differences Between In-Vivo Measurements and In-Silico Calculations

The differences between in-vivo measurements and in-silico calculations of the nasal resistance are well known in the scientific community. Nonetheless, there exists no thorough investigation of the causes for these differences yet. A reason for this might be the quite complex process pipeline for the calculation of the nasal resistance using CFD. In every step of that pipeline uncertainty is introduced. Several aspects of the pipeline are discussed as culprits for the differences observed.

Errors during the image-segmentation procedure could lead to a faulty three-dimensional geometry. If the Hounsfield threshold during the segmentation is chosen too high, the segmented cavity will be wider than the real, patient-specific anatomy. Thus, the resistances in the model would be lower. However, there is currently no specific threshold employed by all working groups using CFD for calculation of nasal airflow. Thresholds from -1000 HU to -200 HU are commonly used. Since no publications report numerically calculated resistance in the range of the in-vivo measurements, it can be assumed, that those variations do not cause the large differences observed. Quadrio et al. also showed that a realistic reconstruction of the nasal cavity is possible using CT resolutions as in the present study [21, 22]. Furthermore, we performed additional simulations, where the geometry of one symptom-free subject was shrinked by shifting the surface geometry inwards along the surface's normal direction. This shrinking of the surface geometry was performed step wise, until a similar pressure drop as in the rhinomanometric measurements was observed. Here, a volume reduction of more than 60 % was necessary to reach flow resistances similar to those from in-vivo measurements. Only the widest passages were still patent, especially the regions parallel to the nasal septum were completely collapsed. Errors of this magnitude are simply not possible with the segmentation procedure employed [21]. While errors might be introduced during the segmentation, they cannot explain the large differences observed.

Another widely discussed culprit is the artificial truncation of the nasal cavity at the nostrils. In most simulations, the ambient surrounding the head is not regarded. However, Taylor et al. reported, that this

truncation has no severe effect on the calculated pressure drop and thus the nasal resistance compared to simulations in which the ambient is considered [29]. Nonetheless, we performed additional simulations, where we incorporated the ambient as well as a mask like it is worn during rhinomanometry. The question was whether the mask alters the inflow into the nasal cavity in a way, that leads to higher pressure drops than free breathing. Again, only a small increase in the nasal resistance was observed, which was too low to explain the large differences between in-vivo measurements and in-silico calculations.

In all studies employing CFD for the calculation of nasal airflow, walls of the nasal cavity were modelled as rigid. Thus, the static pressure acting on the tissue did not result in any movement of the wall. It was discussed that this could be the cause for the differences. Within the nasal cavity, the pressures differences generated by the lung are too low to deform or even collapse tissues such as the pharynx [37, 38]. Even at the nostrils, where movement can be observed during forceful breathing, those movements are small. To ensure that those movements do not result in large changes of the airflow within the nose, two CT scans of the same subject were analyzed. One scan was performed while the subject did not breathe, the second scan was performed during forceful inspiration. There were only slight differences in the geometry and the pressure drop calculated for both geometries differed by 0.4 Pa. Therefore, the movement of tissue due to the static pressure or the Venturi effect can be neglected as cause for the differences observed.

Other aspects discussed as culprits for the large differences are assumptions made in the numerical model of nasal airflow. These include the assumption of laminar or turbulent flow, the simulation of the complete nasal cycle or only quasi-steady time-points for inspiration and expiration, as well as the compressibility of the fluid. However, all these assumptions are well investigated and validated against in-vitro experiments [29].

Therefore, the cause for the differences in nasal resistance remains elusive. A clinical study is planned to better tackle this problem. In this study, the nasal resistance of patients who already received a CT scan of the head will be measured using two different rhinomanometric devices (4RHINO by Rhinolabs GmbH and RHINO-SYS by Happersberger Otopront). The volume flow curves measured using these devices will then be used to perform unsteady simulations. From these simulations the nasal resistance will then be calculated. Furthermore, models of all patient-specific geometries will be manufactured using a 3D printing device (Form 2; Formlabs). In these models the nasal resistance and airflow velocity information will be measured in-vitro. The aim of this study is to gather information from in-vivo and in-vitro measurements as well as in-silico simulations from at least 15 patients. This dataset will then be used to identify causes for the differences in all those methods.

1.7 Conclusion

The computational analysis of nasal airflow allows a spatially and temporally well-resolved insight in nasal airflow. Parameters that could only be measured in-vitro or not at all can be calculated non-invasively using this approach. We were able to show, that the method allows identification of differences in patient-specific flow fields before and after an intervention as well as between symptom-free subjects and symptomatic patients. Using a statistical shape model, we were able to identify regions within the nasal cavity, where wall shear stress distributions differed between symptom-free subjects and symptomatic patients. This demonstrates that the combination of numerical simulation of nasal airflow and statistical shape modelling can provide additional support overcoming the problems caused by the heterogeneity of the nasal cavity.

In theory, the outcome of a treatment could be predicted a priori to the real intervention using CFD. Furthermore, the numerical simulation of patient-specific nasal airflow will - most likely - be an essential tool in understanding perception mechanisms at the nasal epithelium, helping to better differentiate healthy and disturbed nasal airflow.

However, validation of the method against in-vivo measured nasal resistances were not successful. Until now, it is completely unclear, what causes the large differences between in-vivo measurements and in-vivo calculations. Both methods are well understood and thoroughly investigated. Currently, it is not possible to easily reject one of the methods as the erroneous one. While rhinomanometry is established within the clinical routine, its benefit is controversial at Validations against in-vitro experiments also revealed a good agreement in calculated and measured flow patterns.

Therefore, further research is warranted, to tackle the cause of the large differences observed between in-vivo measurements and in-silico calculations of nasal resistances. This question has to be addressed thoroughly for the numerical simulation of nasal airflow to become clinically relevant. I am confident, that the average geometry of the human nasal cavity, which was made freely available [48] is an essential first step to tackle this question, as it provides a common ground for researchers to compare their findings on.

1.8 Literature

[1] M Jessen and L Janzon. “Prevalence of non-allergic nasal complaints in an urban and a rural population in Sweden”. In: Allergy 44 (1989), pp. 582-587.

[2] M Stewart, BJ Ferguson, and L Fromer. “Epidemology and burden of nasal congestion”. In: International Journal of General Medicine 3 (2010), pp. 37-45.

[3] A Shedden. “Impact of Nasal Congestion on Quality of Life and Work Productivity in Allergic Rhinitis: Findings from a Large Online Survey”. In: Treatments in Respiratory Medicine 4(6) (2005), pp. 439-446.

[4] C Bermuller, H Kirsche, G Rettinger, and H Riechelmann. “Diagnostic Accuracy of Peak Nasal Inspiratory Flow and Rhinomanometry in Functional Rhinosurgery”. In: The Laryngoscope 118 (2008), pp. 605-610.

[5] T Hildebrandt, WJ Heppt, U Kertzscher, and L Goubergrits. “The Concept of Rhinorespiratory Homeostasis - A New Approach to Nasal Breathing”. In: Facial Plastic Surgery 29 (2013), pp. 85-92.

[6] G Mlynski and A Beule. “ Diagnostik der respiratorischen Funktion”. In: HNO 56 (2007), pp. 81-99.

[7] K Vogt, KD Wernecke, H Behrbohm, W Gubisch, and M Argale. “Four-phase rhino- manometry: a multicentric retrospective analysis of 36,563 clinical measurements”. In: European Archives of Oto-Rhino-Laryngology online (2015).

[8] S Grutzenmacher, C Lang, and G Mlynski. “The Combination of Acoustic Rhinometry, Rhinoresistometry and Flow Simulation in Noses before and after Turbinate Surgery: A Model Study”. In: ORL 65 (2003), pp. 341-347.

[9] J Lindemann and G Rettinger. S2k-Leitlinie 017/070: Formstorungen der inneren und / oder äußeren Nase. Medizinische Leitlinie. Deutsche Gesellschaft für Hals-Nasen-Ohren- Heilkunde, Kopf und Hals-Chirurgie Chirurgie, 2016.

[10] T Verse, A Dreher, C Heiser, M Herzog, JT Maurer, W Pirsig, K Rohd, N Rothmeier, A Sauter, A Steffen, S Wenzel, and BA Stuck. S2e-Leitlinie 017/069: HNO-spezifische Therapie der obstruktiven Schlafapnoe bei Erwachsenen. Medizinische Leitlinie. Deutsche Gesellschaft fur Hals-Nasen-Ohren-Heilkunde, Kopf und Hals-Chirurgie Chirurgie, 2015.

[11] DEGAM. DEGAM Leitlinie Nr. 10: Rhinosinusitis. Medizinische Leitlinie (wird aktuell überarbeitet) Deutsche Gesellschaft für Allgemeinmedizin und Familienmedizin, 2008.

[12] G Mlynski. “Gestorte Funktion der oberen Atemwege Wiederherstellende Verfahren bei gestörter Funktion der oberen Atemwege. Nasale Atmung”. In: Laryngo-Rhino-Otologie 84 (2005), pp. 101-124.

[13] TH Schiebler and HW Korf. Anatomie. 10th. Springer, 2015.

[14] kowalska-art. Anatomie der Nase und Rachen - Vektor Illustration. stock photo. iStock by Getty Images, 2015.

[15] J Osman, F Großmann, K Brosien, U Kertzscher, L Goubergrits, and T Hildebrandt. “Assessment of nasal resistance using computational fluid dynamics”. In: Current Directions in Biomedical Engineering 2(1) (2016), pp. 617-621.
[16] G Mlysnki and J Low. “Die Rhinoresistometrie — Eine Weiterentwicklung der Rhinomanometrie”. In: Laryngo-Rhino-Otologie 72(12) (1993), pp. 608-610.
[17] TF Groß and F Peters. “A fluid mechanical interpretation of hysteresis in rhinomanometry”. In: ISRN Otolaryngol 2011 (2011), p. 126520.
[18] L Goubergrits, J Schaller, U Kertzscher, N van den Bruck, K Poethkow, C Petz, HC Hege HC, and A Spuler. “Statistical wall shear stress maps of ruptured and unruptured middle cerebral artery aneurysms”. In: J R Soc Interface 9(69) (2012), pp. 677-688.
[19] K Zhao and J Jiang. “What is normal nasal airflow? A computational study of 22 healthy adults”. In: Int Forum Allergy Rhinol 4(6) (2014), pp. 435-446.
[20] K Zhao, J Jiang, K Blacker, B Lyman, P Dalton, BJ Cowart, and EA Pribitkin. “Regional Peak Mucosal Cooling Predicts the Perception of Nasal Patency”. In: The Laryngoscope 124 (2014), pp. 589-595.
[21] M Quadrio, C Pipolo, S Corti, R Lenzi, F Messina, C Pesci, and G Felisati. “Review of computational fluid dynamics in the assessment of nasal air flow and analysis of its limitations”. In: Eur Arch Otorhinolaryngol 271 (2014), pp. 2349-2354.
[22] SK Kim, Y Na, JI Kim, and SK Chung. “Patient specific CFD models of nasal air- flow: overview of methods”. In: J Biomech 46 (2013), pp. 299-306.
[23] JA Sethian. Level Set Methods and Fast Marching Methods: Evolving Interfaces in Compu-tational Geometry, Fluid Mechanics, Computer Vision, and Materials Science. 2nd. Cambridge University Press, 1999.
[24] DL Pham, C Xu, and JL Prince. “Current methods in medical image segmentation”. In: Annu Rev Biomed Eng 2 (2000), pp. 315-337.
[25] WE Lorensen and HE Cline. “Marching cubes:a high resolution 3D surface construction algorithm”. In: Comput Graph 21 (1987), pp. 163-169.
[26] F Moukalled, L Mangani, and M Darwish. The Finite Volume Method in Computational Fluid Dynamics. Steinkopff Verlag, 2007.
[27] K Hemtiwakorn, V Mahasitthiwa, S Tungjitkusolmu, K Hamamot, and C Pintaviroo. “Patient-Specific Aided Surgery Approach of Deviated Nasal Septum Using Computational Fluid Dynamics”. In: IEEJ Trans 10 (2015), pp. 274-286.
[28] JS Rhee, DE Cannon, DO Frank, and JS Kimbell. “Role of virtual surgery in preoperative planning”. In: Arch Facial Plast Surg 14 (2012), pp. 354-359.
[29] DJ Taylor, DJ Doorly, and RC Schroter. “Inflow boundary profile prescription for nu¬merical simulation of nasal airflow”. In: Journal of the Royal Society Interface 7 (2010), pp. 515-527.
[30] AM Gambaruto, DJ Taylor, and DJ Doorly. “Decomposition and Description of the Nasal Cavity Form”. In: Annals of Biomedical Engineering 40(5) (2012), pp. 1142-1159.
[31] Y Liu, MR Johnson, EA Matida, S Kherani, and J Marsan. “Creation of a standardized geometry of the human nasal cavity”. In: Journal of Applied Physiology 106 (2009), pp. 764-795.
[32] K Inthavong, Y Shang, and J Tu. “Surface mapping for visualization of wall stresses during inhalation in a human nasal cavity”. In: Respiratory Physiology and Neurobiology 190 (2014), pp. 54-61.
[33] GJM Garcia, JS Kimbell, and DO Frank-Ito. In Reference to Regional Peak Mucosal Cooling Predicts the Perception of Nasal Patency. Letter to the Editor. The Laryngoscope, 2014.
[34] K Zhao, P Dalton, BJ Cowart, and EA Pribitkin. In Response to Regional Peak Mucosal Cooling Predicts the Perception of Nasal Patency. Letter to the Editor. The Laryngoscope, 2014.
[35] JH Zhu, HP Lee, KM Lim, SJ Lee, LT Li San, and DY Wang. “Inspirational airflow patterns in deviated noses: a numerical study”. In: Comput Methods Biomech Biomed Eng 16 (2013), pp. 1298-1306.

[36] C Xu, S Sin, JM McDonough, JK Udupa, A Guez, R Arens, and DM Wootton. “Computational fluid dynamics modeling of the upper airway of children with obstructive sleep apnea syndrome in steady flow”. In: Journal of Biomechanics 39 (2006), pp. 2006-2054.
[37] CS Park. “Role of Nose in Sleep-Disordered Breathing”. In: Sleep Med Res 5(1) (2014), pp. 1-4.
[38] R Fodil, L Brugel-Ribere, C Croce, G Shirlea-Apiou, C Larger, JF Papon, C Delclaux, A Coste, D Isabey, and B Louis. “Inspiratory flow in the nose: a model coupling flow and vasoerectile tissue distensibility”. In: J Appl Physiol 98 (2005), pp. 288-295.
[39] T Heimann and HP Meinzer. “Statistical shape models for 3D medical image segmentation: A review”. In: Medical Image Analysis 13 (2009), pp. 543-563.
[40] T Heimann. Statistical Shape Models for 3D Medical Image Segmentation. VDM Verlag Dr. Müller, 2008.
[41] D Kainmueller, H Lamecker, S Zachow, and HC Hege. “An articulated statistical shape model for accurate hip joint segmentation”. In: Conference Proceedings IEEE Eng Biol Soc 2009 (2009), pp. 6345-51.
[42] H Lamecker and S Zachow. Statistical Shape Modeling of Musculoskeletal Structures and Its Applications. Springer, 2016.
[43] DAJ Wilson, C Anglin, F Ambellan, CM Grewe, A Tack, H Lamecker, M Dunbar, and S Zachow. “Validation of three-dimensional models of the distal femur created from surgical navigation point cloud data for intraoperative and postoperative analysis of total knee arthroplasty”. In: International Journal of Computer Assisted Radiology and Surgery online (2017).
[44] L Tian, K Inthavong, G Liden, Y Shang, and J Tu. “Transport and Deposition of Welding Fume Agglomerates in a Realistic Human Nasal Airway”. In: Ann Occup Hyg 60(6) (201), pp. 731-747.
[45] A Rygg, M Hindle, and PW Longest. “Absorption and Clearance of Pharmaceutical Aerosols in the Human Nose: Effects of Nasal Spray Suspension Particle Size and Properties”. In: Pharmaceutical Research 33 (2016), pp. 909-921.
[46] J Dong, Y Shang, K Inthavong, J Tu, R Chen, R Bai, D Wang, and C Chen. “Comparative Numerical Modeling of Inhaled Nanoparticle Deposition in Human and Rat Nasal Cavities”. In: Toxicological Sciences 152(2) (2016), pp. 284-296.
[47] GJM Garcia, BM Hariri, RG Patel, and JS Rhee. “The relationship between nasal resistance to airflow and the airspace minimal cross-sectional area”. In: Journal of Biomechanics 49 (2016), pp. 1670-1678.
[48] J Bruening, T Hildebrandt, W Heppt, N Schmidt, H Lamecker, A Zengel, N Amiridze, H Ramm, M Bindernagel, S Zachow, and L Goubergrits. „Characterization of the Airflow within an Average Geometry of the Healthy Human Nasal Cavity”. In: Nature Scientific Reports 10 (2020), pp. 3755.
[49] C Li, G Maza, AA Farag, JP Krebs, B Deshpande, BA Otto, and K Zhao. “Asymptomatic vs symptomatic septal perforations: a computational fluid dynamics examination.”. In: International Forum of Allergy and Rhinology 9 (2019), pp. 883-890.
[50] K Inthavong, P Das, N Singh, and J Sznitman, “In silico approaches to respiratory nasal flows: A review.” In: Journal of Biomechanics 97 (2019), pp. 109434.
[51] EG Wüstenberg, M Scheibe, T Zahnert, and T Hummel. „Different swelling mechanisms in nasal septum (Kiesselbach area) and inferior turbinate responses to histamine: an optical rhinometric study.” In: Arch Otolaryngol Head Neck Surg 132 (2006), pp. 277 – 281.
[52] W Keustermans, T Huysmans, F Danckaers, A Zarowski, B Schmelzer, J Sijbers, and JJJ Dirckx. “High quality statistical shape modelling of the human nasal cavity and applications.” In: Royal Society Open Science 5 (2018), pp. 181558.

2 Eidesstattliche Versicherung

„Ich, Jan Brüning, versichere an Eides statt durch meine eigenhändige Unterschrift, dass ich die vorgelegte Dissertation mit dem Thema „Statistische Untersuchung von statischen Druck und Wandschubspannungsverteilungen der Strömung der Nasenatmung basierend auf der numerischen Strömungsberechnung" selbstständig und ohne nicht offengelegte Hilfe Dritter verfasst und keine anderen als die angegebenen Quellen und Hilfsmittel genutzt habe.

Alle Stellen, die wörtlich oder dem Sinne nach auf Publikationen oder Vorträgen anderer Autoren beruhen, sind als solche in korrekter Zitierung (siehe „Uniform Requirements for Manuscripts (URM)“ des ICMJE - www.icmje.org) kenntlich gemacht. Die Abschnitte zu Methodik (insbesondere praktische Arbeiten, Laborbestimmungen, statistische Aufarbeitung) und Resultaten (insbesondere Abbildungen, Graphiken und Tabellen) entsprechen den URM (s.o) und werden von mir verantwortet.

Meine Anteile an den ausgewählten Publikationen entsprechen denen, die in der untenstehenden gemeinsamen Erklärung mit dem Betreuer, angegeben sind. Sämtliche Publikationen, die aus dieser Dissertation hervorgegangen sind und bei denen ich Autor bin, entsprechen den URM (s.o) und werden von mir verantwortet.

Die Bedeutung dieser eidesstattlichen Versicherung und die strafrechtlichen Folgen einer unwahren eidesstattlichen Versicherung (§156,161 des Strafgesetzbuches) sind mir bekannt und bewusst."

_____	_____
Datum	Unterschrift – Jan Brüning

3 Anteilserklärung

1. **Publikation:** T. Hildebrandt, J. Osman, L. Goubergrits, *Numerische Strömungssimulation – Eine neue Methode zur Beurteilung der Nasenatmung*. HNO. 64:611-618. 2016.

Bei dieser Publikation war ich für die Rekonstruktion der prä- und postoperativen Geometrie der Nasenhöhle des Patienten, an dem die Methode verdeutlicht wurde, zuständig. Ich habe die dreidimensionale Geometrie erstellt und die Strömungssimulationen durchgeführt. Alle Abbildungen in der Publikation sowie die zugrundeliegenden Auswertungen wurden von mir erstellt und durchgeführt. Am Manuskript habe ich ausschließlich bei der Beschreibung der technischen Details (Grundlagen der Durchführung) und der Beschreibung der strömungsmechanischen Parameter mitgewirkt.

2. **Publikation**: S. Bessler, K: Mende, L. Goubergrits, J. Osman, T. Hildebrandt. *The Anterior Spreader Flap: A Minimally Invasive Alternative to the Auto Spreader Flap in the Treatment of Patients with Nasal Valve Dysfunction*. International Journal of Otorhinolaryngology and Head and Neck Surgery. 3:184-189. 2014.

Bei dieser Publikation habe ich die prä- und postoperative Geometrie der Nasenhöhle aus den vorhandenen CT-Daten rekonstruiert und die patientenspezifische Strömung berechnet. Die Auswertung der numerisch berechneten Strömung wurde von mir durchgeführt. Die Abbildungen 4 und 5 wurden von mir erstellt.

3. **Publikation**: J. Bruening, L. Goubergrits, W. Heppt, S. Zachow, T. Hildebrandt. *Numerical Analysis of Nasal Breathing: A Pilot Study*. Facial Plast Surg. 33:388-395. 2017.

Bei dieser Arbeit wurde die Rekonstruktion der 13 patientenspezifischen Geometrien der Nasenhöhle von mir durchgeführt. Ebenso habe ich die Strömungssimulationen durchgeführt. Die Separierung der Nasenscheidewand aus den patientenspezifischen Geometrien wurde ebenso von mir durchgeführt wie deren Ausrichtung anhand der verwendeten Schablone. Weiterhin habe ich die Projektion der Daten und die Berechnung der Mittel- und Medianlandkarten des statischen Druckes und der Wandschubspannungen durchgeführt. Alle Abbildungen bis auf das Histogramm in Abbildung 3 wurden von mir erstellt. Ich war maßgeblich an dem Verfassen des Manuskriptes beteiligt.

4. **Publikation**: J. Osman, F. Großmann, K. Brosien, U. Kertzscher, L. Goubergrits, T. Hildebrandt, *Assessment of nasal resistance using computational fluid dynamics*. Current Directions in Biomedical Engineering. 2(1):617-621. 2016.

Alle patientenspezifischen Geometrien die in dieser Studie untersucht wurden, wurden von mir rekonstruiert. Ich habe die Programme für die Auswertung der rhinomanometrischen Rohdaten geschrieben und die Auswertung der Daten durchgeführt. Alle Simulationen, die für diese Publikation erforderlich waren, wurden von mir durchgeführt. Die Auswertung der Ergebnisse und die Beurteilung dieser im Kontext der Fachliteratur wurden von mir durchgeführt. Weiterhin wurde das Manuskript von mir verfasst und ich war für das Einreichen und die Revision zuständig. Zusätzliche Untersuchungen die nicht in der Publikation aber in der Diskussion der Synopsis erwähnt werden, wurden von mir durchgeführt.

_____	_____
Datum	Unterschrift und Stempel des betreuenden Hochschullehrers
_____	_____
Datum	Unterschrift des Doktoranden

4 Druckexemplare der ausgewählten Publikationen

Im Folgenden werden die vier Publikationen, welche die Grundlage dieser kumulativen Dissertationsschrift bilden, beigefügt. Die Publikationen werden in derselben Reihenfolge aufgelistet, in der sie in der Synopsis beschrieben wurden.

In der digitalen Version dieser Arbeit sind nicht alle Publikationen hinterlegt. Für jene Arbeiten, für die keine Erlaubnis zur Veröffentlichung eingeholt werden konnte, ist jedoch die vollständige Literaturangabe sowie der DOI-Link zur Arbeit angegeben. Um eine Konsistenz bezüglich der Seitenzahlen mit dem gedruckten Exemplar dieser Arbeit zu gewährleisten wurden entsprechende Leerseiten für die fehlenden Publikationen eingefügt.

Publikation I – Seite 1 von 8

T. Hildebrandt, J. Osman, L. Goubergrits, *Numerische Strömungssimulation – Eine neue Methode zur Beurteilung der Nasenatmung*. HNO. 64:611-618. 2016.

DOI: https://doi.org/10.1007/s00106-016-0209-8

S. Bessler, K: Mende, L. Goubergrits, J. Osman, T. Hildebrandt. *The Anterior Spreader Flap: A Minimally Invasive Alternative to the Auto Spreader Flap in the Treatment of Patients with Nasal Valve Dysfunction*. International Journal of Otorhinolaryngology and Head and Neck Surgery. 3:184-189. 2014.

DOI: https://doi.org/10.4236/ijohns.2014.34034

Publikation III – Seite 1 von 8

J. Bruening, L. Goubergrits, W. Heppt, S. Zachow, T. Hildebrandt. *Numerical Analysis of Nasal Breathing: A Pilot Study*. Facial Plast Surg. 33:388-395. 2017.

DOI: https://doi.org/10.1055/s-0037-1603789

J. Osman, F. Großmann, K. Brosien, U. Kertzscher, L. Goubergrits, T. Hildebrandt, *Assessment of nasal resistance using computational fluid dynamics*. Current Directions in Biomedical Engineering. 2(1):617-621. 2016.

DOI: https://doi.org/10.1515/cdbme-2016-0136

5 Lebenslauf

Mein Lebenslauf wird aus datenschutzrechtlichen Gründen in der elektronischen Version meiner Arbeit nicht veröffentlicht.

6 Komplette Publikationsliste

2010

- E. Wellnhofer, J. Osman, U. Kertzscher, K. Affeld, E. Fleck, L. Goubergrits. *Flow simulation studies in coronary arteries – impact of side-branches*. Atherosclerosis, 2010, 213:475-481

2011

- E. Wellnhofer, J. Osman, U. Kertzscher, K. Affeld, E. Fleck, L. Goubergrits. *Non-dimensional modeling in flow simulation studies of coronary arteries including side-branches: A novel diagnostic tool in coronary artery disease*. Atherosclerosis, 2011, 216:277-282.

2014

- S. Bessler, K. Mende, L. Goubergrits, J. Osman, B. Strub. *The Anterior Spreader Flap: A Minimally Invasive Alternative to the Auto Spreader Flap in the Treatment of Patients with Nasal Valve Dysfunction*. International Journal of Otolaryngology and Head \& Neck Surgery, 2014, 3:184-189.

2015

- P. Berg, C. Roloff, O. Beuing, S. Voss, S. Sugiyama, N. Aristokleous, A.S. Anayiotos, N. Ashton, A. Revell, N.W. Bressloff, A.G. Brown, B.J. Chung, J.R. Cebral, G. Copelli, W. Fu, A. Qiao, A.J. Geers, S. Hodis, D. Dragomir-Daescu, E. Nordahl, Y. Bora Suzen, M. Owais Khan, K. Valen-Sendstad, K. Kono, P.G. Menon, P.G. Albal, O. Mierka, R. Münster, H.G. Morales, O. Bonnefous, J. Osman, L. Goubergrits, J. Pallares, S. Cito, A. Passalacqua, S. Piskin, L. Pekkan, S. Ramalho, N. Marques, S. Sanchi, K.R. Schumacher, J. Sturgeon, H. Švihlová, J. Hron, G. Usera, M. Mendina, J. Xiang, H. Meng, D.A. Steinman, G. Janiga. *The Computational Fluid Dynamics Rupture Challenge 2013--Phase II: Variability of Hemodynamic Simulations in Two Intracranial Aneurysms*. Journal of Biomechanical Engineering, 2015, 137(12): 121008.

2016

- J. Osman, F. Großmann, K. Brosien, U. Kertzscher, L. Goubergrits, T. Hildebrandt. *Assessment of nasal resistance using computational fluid dynamics*. Current Directions in Biomedical Engineering 2016, 2(1):617-621.

- T. Hildebrandt, J. Osman, L. Goubergrits. *Numerische Strömungssimulation – Eine neue Methode zur Beurteilung der Nasenatmung*. HNO 2016, 64:611-618.

- L. Goubergrits, J. Osman, R. Mevert, U. Kertzscher, K. Pöthkow, H.C. Hege. *Turbulence in blood damage modeling*. International Journal of Artificial Organs, 2016, 39(4):160-165.

2017

- J.J. Brüning, L. Goubergrits, W. Heppt, S. Zachow, T. Hildebrandt. *Numerical Analysis of Nasal Breathing: A Pilot Study*. Facial Plastic Surgery, 2017, 33:388-395.

- P. Yevtushenko, F. Hellmeier, J. Bruening, T. Kuehne, L. Goubergrits. *Numerical investigation of the impact of branching vessel boundary conditions on aortic hemodynamics*. Current Directions in Biomedical Engineering 2017, 3(2):321–32.

- M. Kelm, L. Goubergrits, J. Bruening, P. Yevtushenko, J. F. Fernandes, S. H. Sündermann, F. Berger, V. Falk, T. Kuehne, CARDIOPROOF group, S. Nordmeyer. Model-Based Therapy Planning Allows Prediction of Haemodynamic Outcome after Aortic Valve Replacement. Nature Scientific Reports,2017, 7:9897

- J.F. Fernandes, L. Goubergrits, J. Brüning, F. Hellmeier, S. Nordmeyer, T. Ferreira da Silva, S. Schubert, F. Berger, T. Kuehne, M. Kelm. *Beyond Pressure Gradients: The Effects of Intervention on Heart Power in Aortic Coarctation*. PLOS ONE, 2017, 12(3): e0174838.

2018

- J. Bruening, F. Hellmeier, P. Yevtushenko, M. Kelm, S. Nordmeyer, S.H. Sündermann, T. Kuehne, L. Goubergrits. Impact of patient-specific LVOT inflow profiles on aortic valve prosthesis and ascending aorta hemodynamics. Journal of Computational Science, 2018, 24:91-100.

- F. Hellmeier, S. Nordmeyer, P. Yevtushenko, J. Bruening, F. Berger, T. Kuehne, L. Goubergrits, M. Kelm. *Hemodynamic Evaluation of a Biological and Mechanical Aortic Valve Prosthesis Using Patient-Specific MRI-Based CFD*. Artificial Organs, 2018, 42(1):49-57.

- K. Valen-Sendstad, A. Bergersen, Y. Shimogonya, L. Goubergrits, J. Bruening, J. Pallares, S. Cito, S. Piskin, K. Pekkan, A. Geers, I. Larrabide, S. Rapaka, V. Mihalef, W. Fu, A. Qiao, K. Jain, S. Roller, K.A. Mardal, R. Kamakoti, T. Spirka, N. Ashton, A. Revell, N. Aristokleous, J.G. Huston, M. Tsuji, F. Ishida, P. Menon, L. Browne, S. Broderick, M. Shojima, S. Koizumi, M. Barbour, A. Aliseda, H. Morales, T. Lefèvre, S. Hodis, Y. Al-Smadi, J. Tran, A. Marsden, S. Vaippummadhom, A. Srinivasan, A. Brown, K. Debus, K. Niizuma, S. Rashad, S. Sugiyama, M. O. Khan, A. Updegrove, S. Shadden, B. Cornelissen, C. Majoie, P. Berg, S. Saalfeld, K. Kono, David Steinman. *Real-World Variability in the Prediction of Intracranial Aneurysm Wall Shear Stress: The 2015 International Aneurysm CFD Challenge*. Cardiovascular Engineering and Technology, 2018. In press.

- P. Berg, S. Voß, S. Saalfeld, G. Janiga, O. Beuing, A.W. Bergersen, K. Valen-Sendstad, J. Bruening, L. Goubergrits, N.M. Cancelliere, D.A. Steinman, T. Lok, A.C. On, Tsang, B.J. Chung, J.R. Cebral, S. Cito, J. Palláres, G. Copelli, B. Csippa, G. Paál, S. Fujimura, H. Takao, S. Hodis, G. Hille, K. Kellermann, M.O. Khan, A.L. Marsden, M. Krestina, H.G. Morales, S. Piskin, E. Finol, H. Rajabzadeh-Oghaz, H. Meng, S. Seshadhri, M. Shojima, S. Sugiyama, K. Niizuma, S. Sergey, T. Wagner, A. Brawanski, Y. Qian, Y. Wu, D.D. Daescu. *Multiple Aneurysms AnaTomy Challenge 2018 (MATCH) - Phase I: Segmentation*. Cardiovascular Engineering and Technology, 2018. In press.

- K. Vellguth, J. Bruening, L. Goubergrits, L. Tautz, A. Hennemuth, U. Kertzscher, F. Degener,M. Kelm, S. Sündermann, T. Kuehne. *Development of a modeling pipeline for the prediction ofhemodynamic outcome after virtual mitral valve repair using image-based CFD*. Int J ComputAssist Radiol Surg, 2018, 13(11), 1795-1805.

- J. Bruening, F. Hellmeier, P. Yevtushenko, T. Kühne, L. Goubergrits. *Uncertainty quantification for non-invasive assessment of pressure drop across a coarctation of the aorta using CFD*. Cardiovascular Engineering and Technology, 2018.

2019

- T. Hildebrandt, J. Bruening, N.L. Schmidt, H. Lamecker, W. Heppt, S. Zachow, L. Goubergrits. *Digital Analysis of Nasal Airflow Facilitating Decision Support in Rhinosurgery*. Facial Plastic Surgery, 2019, 35(1):3-7.

- T. Hildebrandt, J. Bruening, N.L. Schmidt, H. Lamecker, W. Heppt, S. Zachow, L. Goubergrits. *The Healthy Nasal Cavity—Characteristics of Morphology and Related Airflow Based on a Statistical Shape Model Viewed from a Surgeon's Perspective*. Facial Plastic Surgery, 2019, 35(1):9-13.

- L. Goubergrits, F. Hellmeier, J. Bruening, A. Spuler, H.C. Hege, S. Voss, G. Janiga, S. Saal-feldt, O. Beuing, P. Berg. *Multiple Aneurysms AnaTomy CHallenge 2018 (MATCH): uncertaintyquantification of geometric rupture risk parameters*. Biomed Eng Online, 2019, 18(1)

- P. Berg, S. Voß, G. Janiga, S. Saalfeld, A.W. Bergersen, K. Valen-Sendstad, J. Bruening, L.Goubergrits, A. Spuler, T.L. Chiu, A.C.O. Tsang, G. Copelli, B. Csippa, G. Paál, G. Závodszky,F.J. Detmer, B.J. Chung, J.R. Cebral, S. Fujimura, H. Takao, C. Karmonik, S. Elias, N.M.Cancelliere, M. Najafi, D.A. Steinman, V.M. Pereira, S. Piskin, E.A. Finol, M. Pravdivtseva, P.Velvaluri, H. Rajabzadeh-Oghaz, N. Paliwal, H. Meng, S. Seshadhri, S. Venguru, M. Shojima, S.Sindeev, S Frolov, Y. Qian, Y. Wu, K.D. Carlson, D.F. Kallmes, D.Dragomir-Daescu, O. Beuing. *Multiple Aneurysms AnaTomy CHallenge 2018 (MATCH)—phase II: rupture risk assessment*. International Journal of Computer Assisted Radiology and Surgery, 2019.

- K. Vellguth, J. Bruening, L. Tautz, A. Hennemuth, U. Kertzscher, F. Degener, I. Wamala, S. Suendermann, V. Falk, T. Kuehne, L. Goubergrits. *User-dependent variability in mitral valve segmentation and its impact on CFD computed hemodynamic parameters.* International Journal of Computer Assisted Radiology and Surgery, 2019.

- P. Yevtushenko, F. Hellmeier, J. Bruening, S. Nordmeyer, V. Falk, C. Knosalla, M. Kelm M, T. Kuehne, L. Goubergrits. *Surgical aortic valve replacement: are we able to improve hemodynamic outcome?* Biophysical Journal, *2019.*

- I. Wamala, J. Brüning, J. Dittmann, S. Jerichow, J. Weinhold, L. Goubergitis, A. Hennemuth, V. Falk, J. Kempfert. *Simulation of a Right Anterior Thoracotomy Access for Aortic Valve Replacement Using a 3D-Printed Model.* Innovations: Technology and Techniques in Cardiothoracic and Vascular Surgery, 2019.

2020

- J. Brüning, T. Hildebrandt, W. Heppt, N. Schmidt, H. Lamecker, A. Szengel, N. Amiridze, H. Ramm, M. Bindernagel, S. Zachow, L. Goubergrits. *Characterization of the Airflow within an Average Geometry of the Healthy Human Nasal Cavity. Nature Scientific Reports 2020, 10:3755.*